Master of Science in Mathematical Engineering

M.Sc. Thesis

# *Pollutant dynamics in urban street canyons: wind-tunnel experiments and numerical simulations*


**Candidate**

*Marilina Barulli*

**Thesis advisor**

*Prof. Luca Ridolfi*

**Research supervisors**

*Prof. Pietro Salizzoni*

*Dr. Sofia Fellini*


2021/2022

# Contents

# Abstract

The main goal of this study has been to advance the understanding of the effect of the presence of trees on the ventilation of pollutants in an urban geometry. This has been pursued by an experimental campaign conduced in the wind tunnel of the *Laboratoire de Mécanique des Fluides et d'Acoustique* (LMFA) at *École Centrale de Lyon* (ECL). The considered urban geometry consists in a street canyon placed perpendicular to the wind direction within the wind tunnel. Three main configurations of trees were analysed, namely: no trees, two rows of scattered trees and two dense rows of trees. A linear source emitting a mixture of ethane and air has been used to simulate the pollutant. Concentration measurements were performed by means of a Flame Ionization Detector (FID).

To analyse the effect of the vegetation on the dispersion of pollutant, the study has been focused on two aspects: the analysis of the concentration field and the computation of the vertical exchange velocity with the atmosphere above roof level. The obtained results have shown how the presence of trees modifies the pollutant concentration field. In particular, the configuration without trees resulted in a nearly two-dimensional concentration field, while the two configurations with trees presented a three-dimensional field. Furthermore, the results obtained computing the vertical mass transfer velocity did not show any significant difference among the configurations analysed, therefore suggesting that the presence of trees does not affect the overall canyon ventilation.

The study is enriched by the realisation of RANS numerical simulations using *Ansys Fluent.* The obtained results are in a good agreement with the experimental campaign conducted in the wind tunnel. However, due to the inherent constraints of the RANS approach, the numerical results have provided only a qualitative behaviour of the concentration field.

The study has led to new questions and has brought new ideas on the analysis to be done to better understand the dynamics of pollutants in urban canyons.

# Introduction

The urban environment represents an area with particular microclimatic characteristics, due to human activities and to the geometry of the buildings. Urbanization processes can alter the processes of heat, mass and exchange momentum between the ground and the atmosphere. The most important phenomenon is the formation of the so-called heat island, a limited region above the city with higher temperature with respect to that of the surrounding atmosphere. For large cities, increase in temperature can reach, in the hours preceding the day, $4 - 5$ °C (*Figure 1.1*). Among the main reason for the formation of the heat island, there are the absorption of the solar radiation, which is higher for the materials used in the city (concrete, asphalt etc.) with respect to the rural environment, and the reduction of phenomena of evaporation and transpiration that, for a surface protected from vegetation, counteract the increase of temperature.

The positive effects of vegetation on temperature and humidity, known as "urban cool island", are clearly visible during the afternoon and the evening, when the evaporative cooling has a greater impact. Another important aspect is the type of vegetation. Grilo et al., 2020 showed as trees have an impact on mean summer temperature and relative humidity up to a distance of 60 $m$, compared to grass cover which has an effect only up to 10 $m$. Therefore, trees represent the most efficient feature to consider to optimize urban cool island effect. The cooling effect provided by trees depends also on other factors like the leaf colour, the foliage density and the thermal properties. Despite its positive effect on urban microclimate, vegetation can negatively affect the pollutant concentration in urban areas. In fact, vegetation can play a dual role. On one side, foliage helps the deposition and the absorption of pollutants as explained in detail in *Section 1.2*. On the other side, vegetation can cause an obstruction, inhibiting the ventilation in the canyon. Therefore, the central topic of this study is the evaluation of the effect of the trees on the dispersion of pollutants in urban canyons, meaning for street canyon a road characterized by high buildings on the sides. All the phenomena regarding this topic take place in the lower part of the atmosphere, i.e., the troposphere and, in particular, in the layer closest to the Earth's surface known as atmospheric boundary layer (ABL). To this purpose, in Chapter 1 of the present work, a description of the ABL is provided. Then, the influence of vegetation on the dispersion of pollutants is treated from a qualitative point of view, taking into account the characterization of the trees by means of their porosity.  After a summary of the previous studies, results from the present experimental campaign and from the present numerical simulations will be presented in Chapter 2 and Chapter 3 respectively.

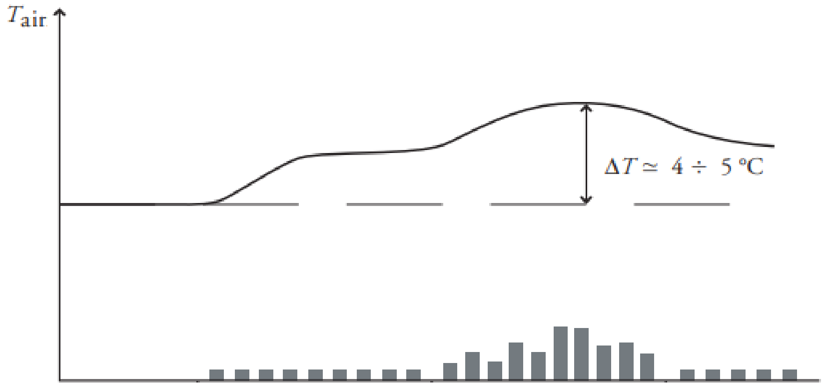


***Figure 1.1*** – Increase in temperature due to the presence of the urban canopy: heat island (Cancelli et al., 2006).

# 1. Theoretical concepts and previous studies

## 1.1 The atmospheric boundary layer

The atmospheric boundary layer, also called planetary boundary layer (PBL), is the tropospheric layer directly influenced by the presence of Earth's surface and it is characterised by turbulent exchanges of momentum, heat, and mass. The depth of the ABL changes depending on the atmospheric conditions. During the night a reduction of the ABL is visible, caused by the cooling of the ground which inhibits the vertical dispersion. Similarly, during the day, the heating of the surface promotes convective motions causing an extension of the ABL. Meteorological conditions like cloudiness or wind affect the depth of the ABL also. In particular, cloudiness reduces the effect of solar radiation during the day and wind promotes the mixing between different layers, bringing to a homogenization of the temperature field all over the boundary layer.

### 1.1.1 Wind profile in the atmospheric boundary layer

The ABL can be subdivided into different layers, as shown in *Figure 1.1.1.* Starting from the bottom there is the layer occupied by the urban canopy, where the flow depends on buildings geometry and orientation. Above this one, roughness sub-layer is present, where the flow is strongly influenced by the presence of buildings. This layer ends up at the so-called blending height $z_*$ where the flow perceives the presence of the buildings as a single indistinct element of aerodynamic resistance, evenly distributed on the surface. Then, the inertial layer is present. Here the horizontal mean wind speeds can be described using the semi-empirical law

$$U(z) = \frac{u_*}{k} ln\left(\frac{z-d}{z_0}\right) \tag{1.1}$$

where:

- $u_*$ is the friction velocity which expresses the shear stress in terms of velocity;
- $z_0$ is the roughness length and it corresponds to the height at which the wind speed theoretically becomes zero;
- $d$ is the zero-plane displacement which represents the vertical displacement of the horizontal plane where wind velocity is assumed to be zero;
- $k = 0.4$ is the Von Karman constant.

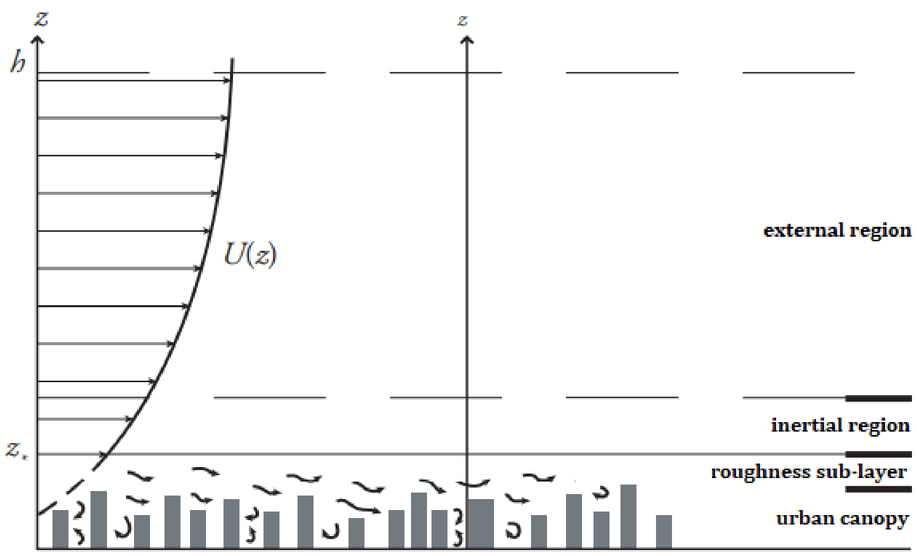


*Figure 1.1.1* – Subdivision of the ABL (Cancelli et al., 2006).

To characterize logarithmic profile and determine the three parameters of the logarithmic law in an experimental campaign, velocity measurements can be carried out. Known the velocity profile and the velocity correlation profile from the measurements, it is easy to estimate the friction velocity as

$$u_* = \sqrt{\overline{-u'w'}}, \tag{1.2}$$

identifying the height interval where $\overline{-u'w'}$ can be considered as constant and using this constant value.

Then, rewriting the (1.1) as

$$z = z_0 \cdot e^{\frac{ku}{u_*}} + d, \tag{1.3}$$

it is easy to obtain $z_0$ and $d$ by means of a linear regression.

## 1.1.2 Dispersion in the atmospheric boundary layer

From a theoretical point of view, the dispersion of a passive scalar into a turbulent flow field can be studied using the advection-diffusion equation, derived from a pollutant mass conservation

$$\frac{\partial c}{\partial t} = -\nabla \cdot (\boldsymbol{u}c) - \nabla \cdot (D_m \nabla \mathrm{c}), \tag{1.4}$$

where $c$ is the passive scalar concentration, $\boldsymbol{u} = u(x, y, z, t)$ is the instantaneous velocity field, and $D_m$ the molecular diffusion coefficient. Using Reynolds decomposition and applying Reynolds average operator all over the equation, as presented in details in $Section$ 3.1, the equation written in components becomes

$$\frac{\partial \overline{c}}{\partial t} = -\frac{\partial}{\partial x_j}\left(\overline{u_j' c'} + \overline{u_j}\,\overline{c}\right), \tag{1.5}$$

where $\overline{u_j' c'}$ is the turbulent flux of passive scalar and $\overline{c}$ is the mean scalar concentration. At this step, the molecular diffusion has been neglected because its effects on the concentration field became significative only on very large time scale compared to the advection time scale. Nevertheless, the obtained equation cannot be solved because of the term containing the turbulent flux which is unknown. One way to solve the equation consists in modelling this term using Fick's law for turbulent fluxes in analogy with molecular fluxes, introducing the turbulent diffusion tensor $K_{ij}$

$$\overline{u_j' c'} = -K_{ji} \frac{\partial c}{\partial x_i}. \tag{1.6}$$

With this assumption, the equation becomes

$$\frac{\partial \overline{c}}{\partial t} = -\frac{\partial}{\partial x_j}\left(-K_{ji} \frac{\partial c}{\partial x_i} + \overline{u_j}\, \overline{c}\right), \tag{1.7}$$

which can now be solved imposing simple boundary conditions. One of the possible solutions for this equation is a Gaussian function which gives the spatial distribution of the time-averaged scalar concentration. Actually, due to the hypothesis on the turbulent fluxes, this solution is only suitable for turbulent flows not disturbed by obstacles and so characterised by simple flow structures.

In an urban geometry, the presence of obstacles like buildings or vegetation has a strong effect on the pollutant dispersion and on the flow field in general. For this reason, the study of dispersion in an urban environment can only be assessed by means of numerical models, parametric models or laboratory experiments. Among the numerical models it is possible to identify three main approaches: DNS (Direct Numerical Simulation), LES (Large Eddy Simulation) and RANS (Reynolds-Averaged Navier-Stokes) simulation. The DNS approach is almost never feasible for flows in complex geometry involving walls and obstacles. This problem is due to the presence of complex structures involving a large range of turbulence scales and to the fact that a direct numerical simulation resolves all these scales. This bring a too high computational cost. On the other hand, RANS approach is really suitable from a computational point of view because no turbulence scale is resolved, but only the effect of these scales on the mean flow modelled. Nevertheless, the RANS approach, as the results in this study will show, do not furnish accurate results for this kind of flow. In fact, only a qualitative description of the flow field is obtained, neglecting the structures involved in the real case. Finally, the LES approach represents a good compromise between accuracy of the results and computation cost. In fact, a large eddy simulation, resolves all the largest scales which contain the great part of the total energy and models the smallest scales that represents the bigger part of computational cost. The models used to simulate these smallest scales, and more in general all the models used to simulate the physical phenomena which are not explicitly resolved, need to be validate. Laboratory experiments represent an important and useful mean to that purpose. Moreover, through the experiments it is possible to study complex phenomena such as the interaction between thermal effects and dispersion. Despite this, the experiments allow the study of a limited number of configurations, due to the difficulty in changing the setup and they allow to estimate all the quantities in far fewer points with respect to a numerical simulation.

Finally, on a larger scale, like for example for an urban geometry of hundreds of streets, parametric models are used. These models evaluate pollutant mass exchanges within the single streets and then interconnect them to obtain a model for the whole urban canyon.

## 1.2 Impact of vegetation

As already mentioned in the introduction to this work, vegetation plays an important role in the study of dispersion, absorption and deposition of pollutant in urban canyons. In general, it has a large positive impact on the urban micro-climate due to the ability to absorb thermal energy through the evapotranspiration process, i.e., the loss of water as vapour form a plant into the atmosphere. However, vegetation can cause an obstruction in urban areas which causes an increase of pollutant concentration, affecting in this way the pedestrian health. The study of these positive or negative effects is therefore important to help urban planners in designing in an efficient way the future urban areas.

## 1.2.1 Dispersion, absorption and deposition of pollutants

Deposition occurs when pollutants are deposited on Earth's surface through rain, clouds, or as dry particles. The pollutant concentration and the way in which the deposition happens, affect the amount of deposition received. Anyway, other factors like meteorology and topography play an important role. In fact, for instance, high wind velocities inhibit the process of deposition causing a continuous recirculation and re-suspension of pollutants, instead, rain washes off the deposited pollutant preventing their reintroduction in the air. The main parameter to quantify the effect of deposition is the deposition velocity defined as the ratio between the mass flow rate of pollutant through the deposition surface and the total pollutant concentration. The main aspects influencing this parameter are:

- dimension of particles: from the biggest to the smallest particles, the main mechanisms involved are sedimentation, interception, impaction, and Brownian motion. Sedimentation refers to the fall of particles due to gravity. Interception happens when the particle are big enough to follow the streamlines but if they flow to close an obstacle, like the branch of a tree, they collide. Impaction involves particles too small to follow the streamlines due to inertia. Finally, Brownian motion involves the smallest particles and, in this case, deposition involves diffusion and obeys to Fick's first and second laws;
- air humidity: this aspect can be traced back to particles dimension. In fact, with high air humidity, particles absorb more water increasing their size;
- presence of vegetation: vegetation represents one of the possible deposition surfaces. The type of vegetation plays a significative role. In fact, vegetation with complex spatial structures tends to allow higher particles deposition.

Concerning the pollutant dispersion in urban areas instead, the main factors to consider are relied to vegetation and to its disposition into the urban geometry. In particular, the main aspects are:

- trees crown dimension: large crowns inhibit the air exchange, reducing the dispersion and increasing the concentration;
- disposition of trees: more spaced trees allow a better recirculation, avoiding the stagnation of pollutants in the street.
- trees porosity: this relates to the permeability of the trees. Low values of porosity identify stronger obstacles which can obstruct the flow causing an accumulation of concentration.

### 1.2.2 Characterization of trees

One of the main aspects to consider for the characterization of the trees and their influence on the flow field and on the dispersion of pollutants is the crown porosity. The porosity of a tree can be described essentially in two ways:

- optical porosity $\beta$ defined as the ratio between the surface not physically occupied by the crown and the total surface of the crown, including the empty areas. This definition is not really significant from a physical point of view but is easy to compute by elaboration of digital photos and gives an indication of the blocking effect caused by the tree;
- aerodynamic porosity $\alpha$ which can be evaluated in two ways. The first method uses an empirical relationship validated by [Guan et al., 2003] which relates aerodynamic porosity to optical porosity

$$\alpha = \beta^{0.4}. \tag{1.8}$$

The second method involves velocity measurements in the wind tunnel. In particular, the trees are inserted in an air stream and upwind and downwind velocities are computed. Then, aerodynamic porosity is given by the relation

$$\alpha = \frac{\int_A U(x,y,z)dA}{\int_A U_0(x,y,z)dA}, \tag{1.9}$$

where $A$ is the frontal area of the crown, $U$ is the mean velocity within the trees and $U_0$ is the approaching wind velocity.
In this study, the computation of optical porosity done in (De Giovanni, 2019) will be used in the following for the realization of numerical simulation in Ansys Fluent, where the porous media are modelled using this definition.

## 1.3 Previous studies

Vegetation inserted within urban canyons may act as obstacles to air ventilation and pollutant dispersion mechanisms, as from the aerodynamic point of view trees are porous objects that may produce changes in drag and wakes to the airflow that crosses their crowns. The effect of tree avenues on the flow and concentration fields inside in urban street canyons has been investigated mainly with wind tunnel experiments and CDF simulations. (Gromke and Ruck, 2007) performed a first experimental campaign inside an isolated street canyon with a row of model trees with spherical crowns placed along the centre axis. They found that, if a wind flow perpendicular to the canyon is considered, the presence of trees causes an increase of pollutant concentration at the pedestrian level at the upwind wall, as trees inhibit the upward flow, and a decrease at the downwind wall, since tree crowns hinder the re-entrainment of the flow from the upwind wall to the downwind one. Moreover, the lateral air exchange promoted by corner eddies is significantly reduced, resulting in an overall increase of the pollutant concentration inside the canyon. The tree induced concentration changes were found to be more pronounced with higher vegetation density, or rather with greater tree crown diameter and smaller tree spacing. The influence of crown porosity has been studied as well, in a second experimental campaign (Gromke and Ruck, 2009), where the tree avenue has been modelled with a lattice cage filled with filament synthetic wadding material of different densities. The results revealed that the influence of the crown porosity on the concentration variations is remarkable only if the pore volume is greater than 97 %. Moreover, velocity measurements show that the presence of a central tree avenue does not destroy the canyon vortex structure, but it reduces the upward and downward flow velocities, resulting in a weakening of the air circulation inside the canyon. By setting different directions of the approaching wind flow (Gromke and Ruck, 2012), it has been found that the presence of tree avenues does not influence the pollutant concentration in the case of wind flow parallel to the street canyon axis, and that with a wind flow inclined 45° with respect to the canyon axis the walls averaged concentration is lower with higher vegetation density, as a more packed vegetation enhances the street axis channelling of the flow. The experimental data, acquired in the street canyon with two rows of trees modelled with the lattice cage, has been used to validate RANS simulations in (Gromke et al., 2008) and (Buccolieri et al., 2009). Numerical simulations reproduce well the flow and concentration fields detected during the experimental campaign, as well as the relative difference in the spatial distribution of the concentration between empty and vegetated street canyons. However, high concentration values at the upwind wall are slightly underestimated, while the lower ones at the downwind wall are well estimated. On the trail of the studies of Gromke et at., the aerodynamic behaviour of vegetation inside urban street canyons has been analysed using the wind tunnel facilities, built in the École Centrale de Lyon. Tree avenues have been modelled arranging plastic small-scale trees in two parallel rows inside the canyon. Different vegetation densities have been reproduced placing the trees with different spacing. Fellini (2021) and De Giovanni (2019) studied the influence of vegetation density and wind direction on the dispersion of passive scalar within a street canyon of $H/W = 0.5$, with street intersections. With the wind blowing perpendicular to the canyon, the results found in the studies cited above have been confirmed: lower pollutant concentration at the downwind wall and higher one towards the upwind wall, decrease in concentration towards the edges due to the action of the corner eddies, overall increase of pollutant concentration, mostly at the upwind wall and canyon edges, with the increase of tree density. The rotation of the model street canyon 60° with respect to the wind direction leads to an accumulation of the pollutant at the edge of the canyon opposite to the one where the flow enters. The presence of trees seems to reduce the longitudinal ventilation, but the influence of the tree density is no more detectable. The overall concentration inside the rotated canyon is half the one measured inside the canyon oriented perpendicular to the wind direction. Moreover, the estimation of the efficiency of the ventilation inside the street canyon has been performed calculating the vertical exchange velocity. Assuming steady-state conditions inside the canyon and that the vertical exchange velocity and the lateral one are equal, in (Salizzoni et al., 2009) and (Fellini et al., 2020) the mass transfer velocity $U_d$ between the canyon and the external flow, with a perpendicular wind direction, has been extracted from the mass balance

$$Q_{et} = \overline{c}U_dLW + 2(\overline{c}U_dWH) \tag{1.10}$$

where $Q_{et}$ is the ethane flow rate emitted inside the canyon from a linear source on the ground, $\overline{c}$ is the spatial mean concentration, $L$ is the length of the control volume, $W$ is the width of the canyon and $H$ its height. It has been found that $U_d$ decreases with the increase of the number of trees, meaning that vegetation reduces the ventilation efficiency of the canyon. However, the contribution of the lateral inflows plays a key role in the dilution of pollutants inside the canyon, thus neglecting the contribution of the lateral mean flow to the street canyon ventilation constitutes an inaccurate estimation of the $U_d$, especially in the empty canyon. To avoid lateral interactions between the external flow and the canyon flow, a street canyon, oriented perpendicular to the wind direction, without street intersections has been analysed in a second experimental campaign (Balestrieri, 2021). Here, the vertical exchange velocity at the rooftop of the canyon has been calculated in a direct way, performing coupled velocity-concentration measurements. The $U_d$ has been calculated as

$$U_d = \frac{1}{\overline{c}LW}\int_A (\overline{wc} + \overline{w'c'})dA \tag{1.11}$$

where $\overline{wc}$ is the mean mass flux, $\overline{w'c'}$ is the turbulent mass flux, $A$ is the area of the rooftop of the canyon. By numerically integrating the total mass flux at the rooftop, they found that the presence of trees enounces the vertical flow rate. This result, opposite to the expectations, has been attributed to the fact that without trees there is a non-negligible lateral outflow, which decreases the overall vertical flow. This hypothesis has been verified, as the expected decrease of $U_d$ in presence of trees has been obtained by imposing that the existing vertical flowrate is equal to the entering one, neglecting any lateral mass exchange. Looking at the variation of the mean passive scalar concentration along the longitudinal direction in the canyon, it has been observed that the concentration field is bi-dimensional in the no-trees configuration, while it is three-dimensional when trees are inserted. This result has been reconducted to the inhomogeneity of the total vertical mass flux in the case of the vegetated canyon: it is maximum in the centre of the canyon, where the mean concentration presents a minimum, and it decreases moving towards the canyon edges, where an accumulation of pollutant has been found. The uncertainty of the estimation of the vertical mass fluxes and the interesting result obtained comparing the concentration fields of the empty canyon with the one of the vegetated canyon, have promoted a further experimental campaign inside a street canyon, again oriented perpendicular to the wind direction, confined both laterally and longitudinally. This configuration is the subject of the present study.

# 2. Experimental investigation

In this section, the setup and the results of the experimental campaign will be presented. The experimental campaign has been carried out in the wind tunnel of the Laboratoire de Mécanique des Fluides et d'Acoustique at the École Centrale de Lyon.

## 2.1 Experimental setup

The wind tunnel used for the experimental campaign consists in a recirculating structure 24 $m$ long, 7.2 $m$ wide and 7.4 $m$ high. The measurement section, framed in red in *Figure 2.1.1*, is 12 $m$ long, 3.5 $m$ wide and 2 $m$ high. It consists of a test section in which the setup of the experiment takes place, a heat exchanger system which allows to keep a desired temperature value, a fan which produces stable velocities in the range $0.5 - 6\ m/s$, a diverging system and a converging system and an upwind grid which allows the developing of a homogeneous turbulence. A sketch of the wind tunnel is represented in the upper part of *Figure 2.1.1*.

The realised setup, shown in *Figure 2.1.2,* consists in an urban environment with rows of buildings represented by means of polystyrene blocks 50 $cm$ long, 50 $cm$ wide and 10 $cm$ high. The distance between two blocks is 20 $cm$. Every block has been covered with bolts 5 $mm$ high to increase the roughness of the surface in order to accelerate the full development of the boundary layer. A photo of the setup is reported at the centre of *Figure 2.1.1*. At the bottom of *Figure 2.1.1*, a sketch of the top view of the cavity where the measurements are taken is reported. This cavity represents an urban canyon with a length-to-width ratio of 2.5 and a height-to-width ratio of 0.5, and it contains the ethane linear source at the ground which is 40 $cm$ long and 1 $cm$ wide. The ethane represents the pollutant, and it is used as a passive tracer since its density is close to that of the air. For this reason, the ethane results to be neutrally buoyant allowing the study of only advection and diffusion phenomena. The source emits a mixture of air and ethane equal to 4 $l/min$ with a volume percentage of ethane equal to 10 %. The release velocity is 0.017 $m/s$ w

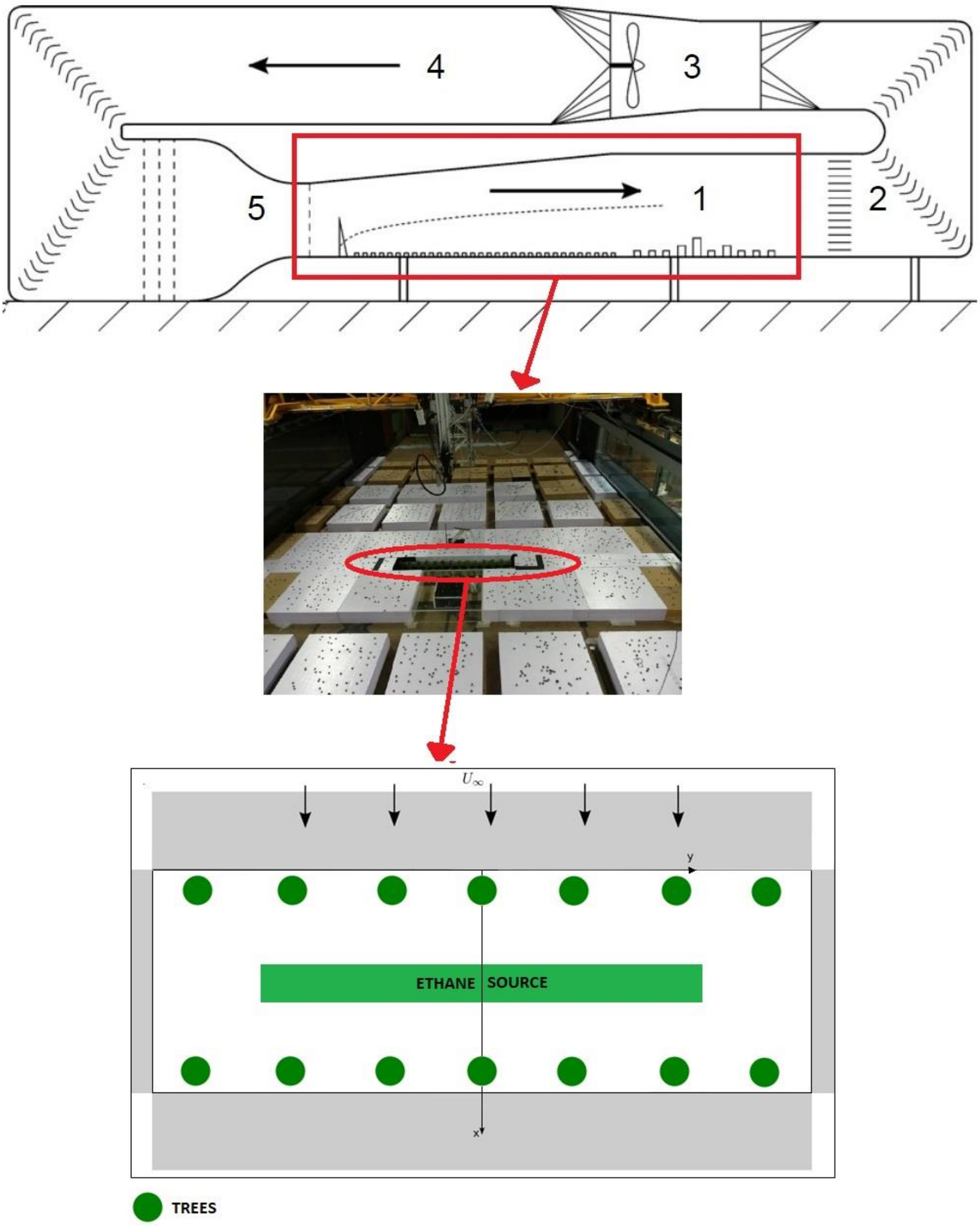


***Figure 2.1.1***– *Sketch of the wind tunnel (top) with test section (1), heat exchanger system (2), fan (3), diverging system (4), converging system and generating turbulence grid (5). Photo of the test section (centre) and sketch of the top view of the cavity (bottom) where the measurements are taken.*

is low enough to not affect the motion field in the canyon.

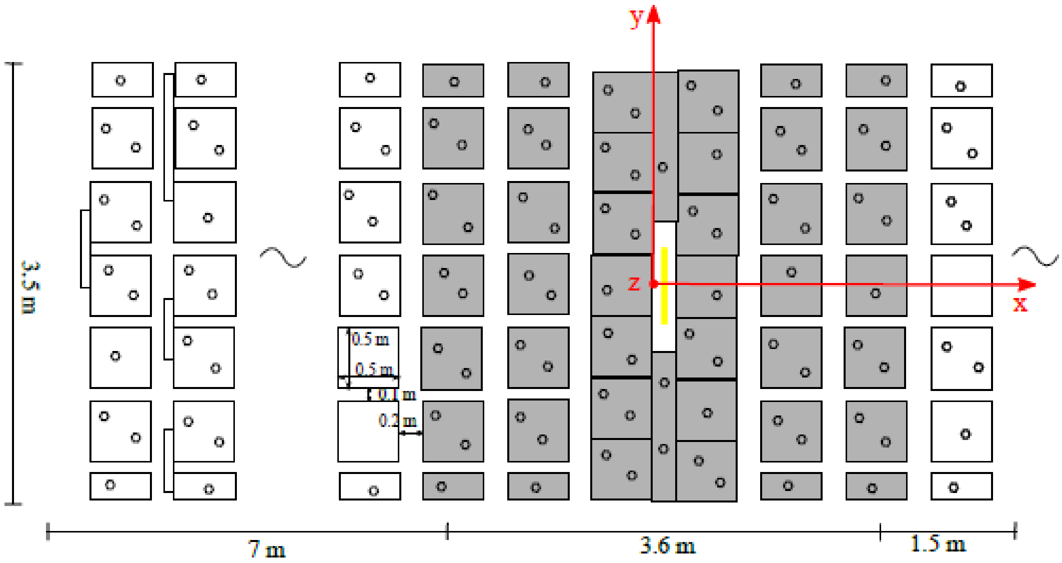


*Figure 2.1.2– Sketch of the experimental setup realized in the test section of the wind tunnel.*

The trees in the cavity are 8.5 *cm* high (considering both crown and trunk), 4.5 *cm* wide and 4.5 *cm* deep. Their porosity has been experimentally evaluated computing the aerodynamic porosity $\alpha$ and the optical porosity $\beta$, as described in section 1.2.2, obtaining respectively $\alpha = 0.29$ and $\beta = 0.95$.

The measurements have been carried out for three different configurations. The first configuration considered is the urban canyon without the trees. Then, two different configurations with trees have been considered changing the number of trees from two rows of seven trees to two rows of fourteen trees. In the following, the three configurations will be referred to respectively as "zero" configuration, "half" configuration and "full" configuration as shown in *Figure 2.1.3*.

*Figure 2.1.3* shows the points in which the measurements have been carried out for the three configurations. In the configurations with trees, measurements have been taken in the central part of the canyon only, right on the ethane source, due to the physical constraint represented by the presence of trees.

Furthermore, in the "full" configuration, more measurements have been carried out to better characterize the concentration field near the maximum values (as will be shown in *Section 2.3*).

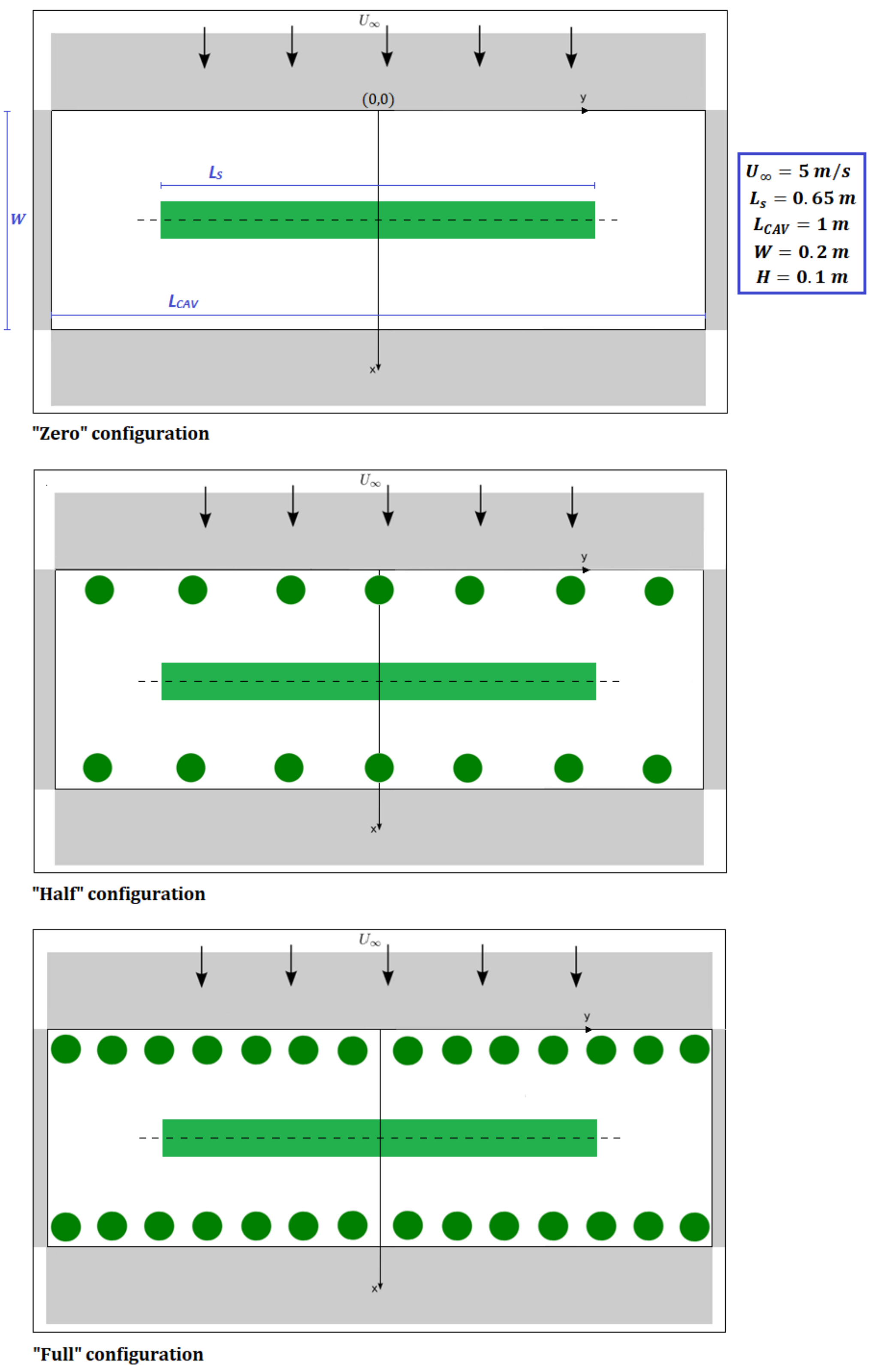


***Figure 2.1.3*** *– Sketch (top view) of the three configurations considered. The green dots represent the threes and the green bar the ethane source at the ground.*

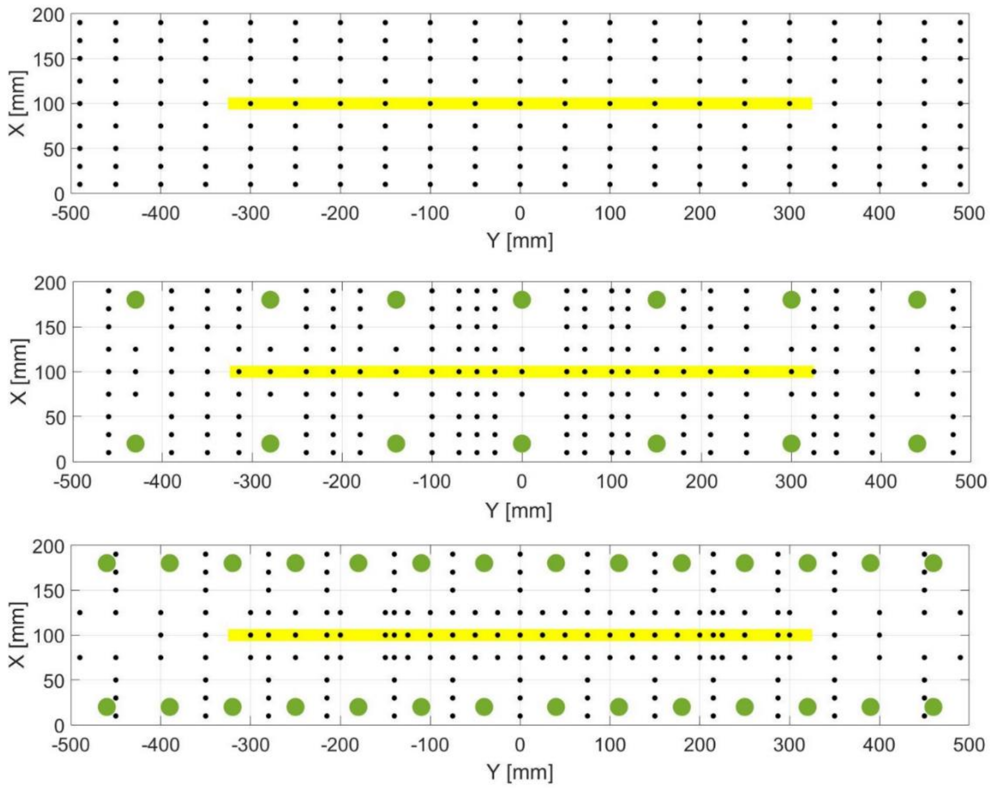


*Figure 2.1.3 – Measurement points for the three configurations considered. From top to bottom, "zero", "half" and "full" configurations respectively. The yellow bar represents the ethane source, and the green dots represent the trees.*

In order to develop the boundary layer along the test section, the wind flow is perturbed by the turbulence grid, by a row of 7 Irwin spires, both placed at the entrance of the test section and by the bolts placed on the buildings. The combination of these elements guarantees a fully developed boundary layer of depth $\delta = 1.1\ m$. The velocity of the fan determines the constant wind velocity in the upper part of the boundary layer which is maintained at $U_\infty = 5\ m/s$. It is controlled by a Pitot tube, which measures the velocity by linking it to the difference between the total pressure and the static pressure, and the fluid density, through the Bernoulli's principle.

In (Balestrieri, 2021), velocity measurements at different distances along wind direction have been carried out to verify the presence of a well-developed boundary layer in the wind tunnel. Then, using the procedure explained in *Section 1.1.1* an estimation of $u_*$, $z_0$, and $d$ has been done to reconstruct the logarithmic wind profile.

*Figure 2.1.4* shows the four different points in which vertical wind profiles has been measured in proximity of the canyon.

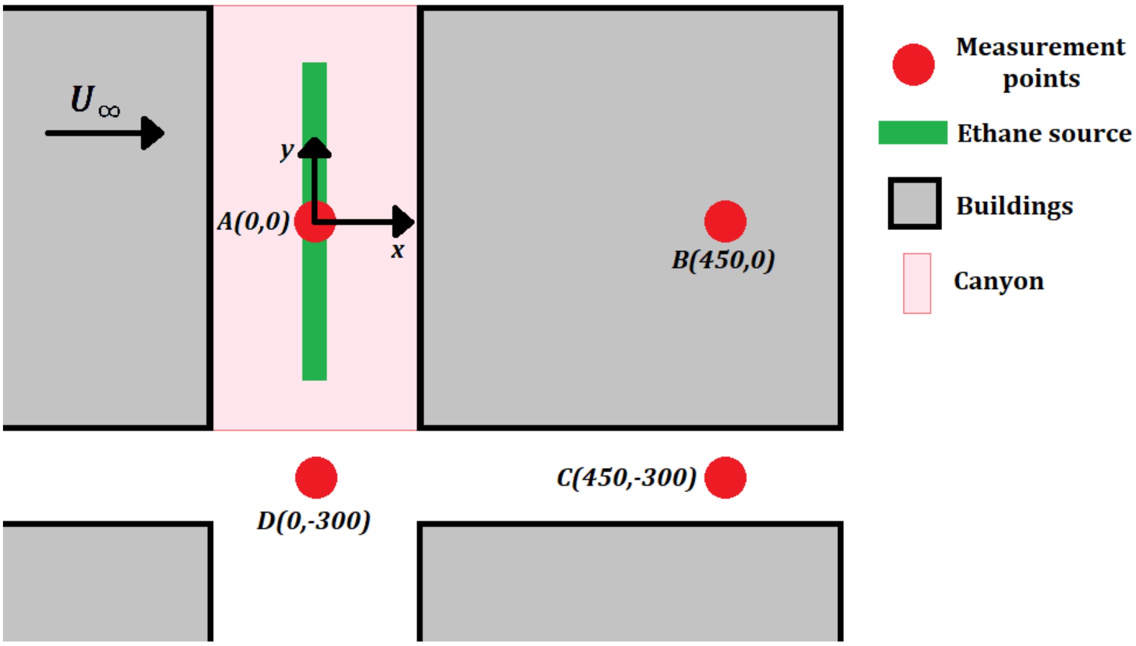


***Figure 2.1.4***– *Sketch of a portion of the setup in the wind tunnel with the points considered to estimate the vertical wind profiles in proximity of the cavity.*

The interest in considering these four points lies in the fact that they identify four different regions of the urban geometry. In fact, the points A, B, C, D represent respectively the canyon, the top of the building, the street between two buildings, and the intersection between two streets.

It is important to have pretty similar velocity profiles in these points to assure the independence of the field from the urban canopy. To complete the analysis the same measurements have been carried out for four distances along wind direction. At each distance, the profiles at the four points A to D have been averaged. The characterization of logarithmic profiles has ended up with $u_* = 0.23\ m/s$, $z_0 = 0.21\ mm$ and $d = 96\ mm$. However, in this previous experimental campaign it was $U_\infty = 5.3\ m/s$, slightly different from the one of the present study. Knowing that the shape of the boundary layer is the same in both experimental campaigns and that the ratio $u_*/U_\infty$ (equal to 0.043) remains constant, in the present study $u_* = 0.22\ m/s$ is obtained.

## 2.2 Measurement instruments

### 2.2.1 Flame Ionisation Detector

Concentration measurements have been carried out using a Flame Ionisation Detector (FID). This instrument is composed of a tube, as thin as possible to not perturb the flow, which sucks the air in the measurement point and injects it in a combustion chamber. At this step, the combustion of the organic compound starts into a hydrogen flame and products ions. These ions are detected and the proportionality between the number of ions and the concentration of the compound is used to measure the concentration itself. The detection of ions is possible by means of two electrodes (a positive and a negative one) that generate a potential difference and so a current. The instrument is very sensible to temperature in surrounding environment and for this reason a calibration has been done at the beginning and at the end of each measurement session to control the accuracy of the measurements. The acquisition time for each point has been of $120\,s$ which is enough to ensure the convergence of the measure as emerged from convergence analysis done in (De Giovanni, 2019).

### 2.2.2 Laser Doppler Anemometer

To characterize the velocity field inside the cavity a Laser Doppler Anemometer (LDA) has been used. It is an optical instrument which operating principle is based on the Doppler effect. The LDA is equipped with an optical system that emits two laser rays, one with the characteristic wavelength of the blue and the other with the characteristic wavelength of the green, which are in turn split into two beams. These beams intersect in a point, which defines the measuring volume, and generate a set of straight fringes. The particles transported inside a fluid cross this set of fringes causing a reflection collected by a photodetector which converts the scattered light into an electrical signal. Subsequently, this signal is converted into a velocity measurement through the Burst Spectrum Analyser (BSA). Each couple of laser beams measure one component of the velocity vector therefore, to measure the third one it is necessary to combine the LDA with a mirror, that deflects the scattered laser beam. Inside the test section, a fog flow is spread, to make the air opaque, to promote reflection, and to provide tracing particles. *Figure 2.2.1* shows a photo of the LDA.

As the measurement occurs when particles intercept the intersection point of the four beams, the acquisition frequency of the instrument is not constant, but it depends on the particle arrival time. Moreover, faster particles are detected more frequently than slower ones. Therefore, to obtain a correct estimation of the statistical moments, it is necessary to weigh them with the particle transit time. Concerning the convergence analysis, as show in (Balestrieri, 2021), 350 000 particles are enough to obtain a good convergence of the measurements.

The measurements have been acquired over a central vertical section, according to five longitudinal profiles at $Z = 20,\ 40,\ 60,\ 80,\ 98$ mm.

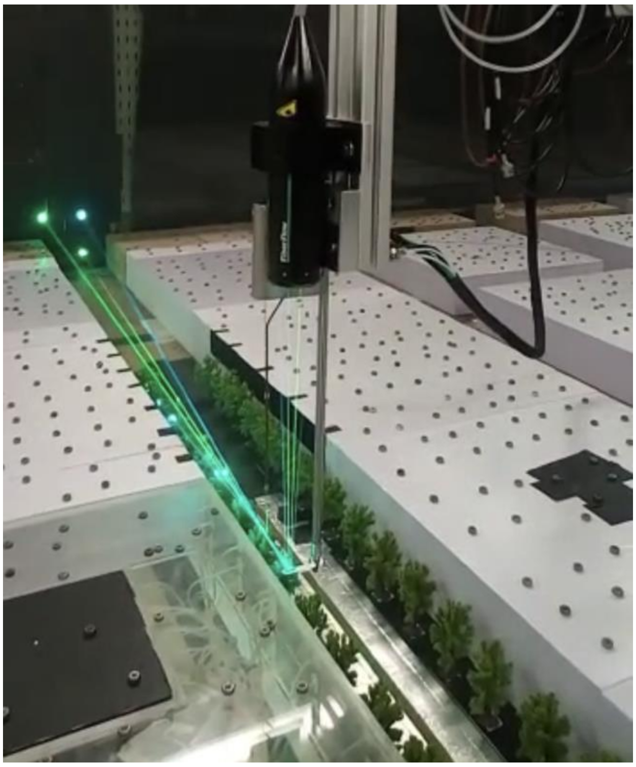

*Figure 2.2.1 – LDA performing velocity measurements in the canyon.*

It was not possible to measure the velocity on a grid as refined as the one used for concentration measurements, because the vegetated canyon cannot host the mirror so inside it is possible to measure velocity between the two rows of trees only.

## 2.3 Results

In this section, results from the experimental campaign will be presented for the three configurations shown in *Figure 2.1.3*.

### 2.3.1 Concentration measurements

In the following, all the concentration measurements will be reported in their dimensionless form using the relation

$$c^* = \frac{\overline{c} U_\infty L_s \delta}{Q_{et}}, \tag{2.1}$$

where $\overline{c}$, measured in $ppm$, is the concentration obtained from the measurements, $U_\infty = 5\ m/s$ the horizontal velocity at the top of the boundary layer, $L_s = 0.65\ m$ is the length of the ethane source, $\delta = 1.1\ m$ is the height of the boundary layer, and $Q_{et} = 0.2\ l/min$ the ethane flow rate of the source.
*Figure 2.3.1* shows the concentration field at different sections along x direction, i.e., the wind direction, for the “zero” configuration. The picture shows as the concentration decreases moving away from the upwind wall, suggesting an accumulation of pollutant in the upwind corner of the cavity. The concentration field shows homogeneity along y direction over the ethane source. This homogeneity is lost when the trees are added, as shown in *Figure 2.3.2 and Figure 2.3.3* where the same sections for the “half” and “full” configurations respectively are represented. When trees are present, the concentration field seems to be organised in two different structures, characterized by two peaks of concentration. The “full” configuration shows a particular symmetry with respect to $y = 0\ mm$ in each section. This symmetry is less evident in the “half configuration” where a less marked structure appears approximately at $y = 300\ mm$. This difference can be due to the different position of the trees in the two configurations. In fact, in the “half” configuration one of the trees is placed exactly at $y = 0\ mm$, breaking in this way the symmetry.

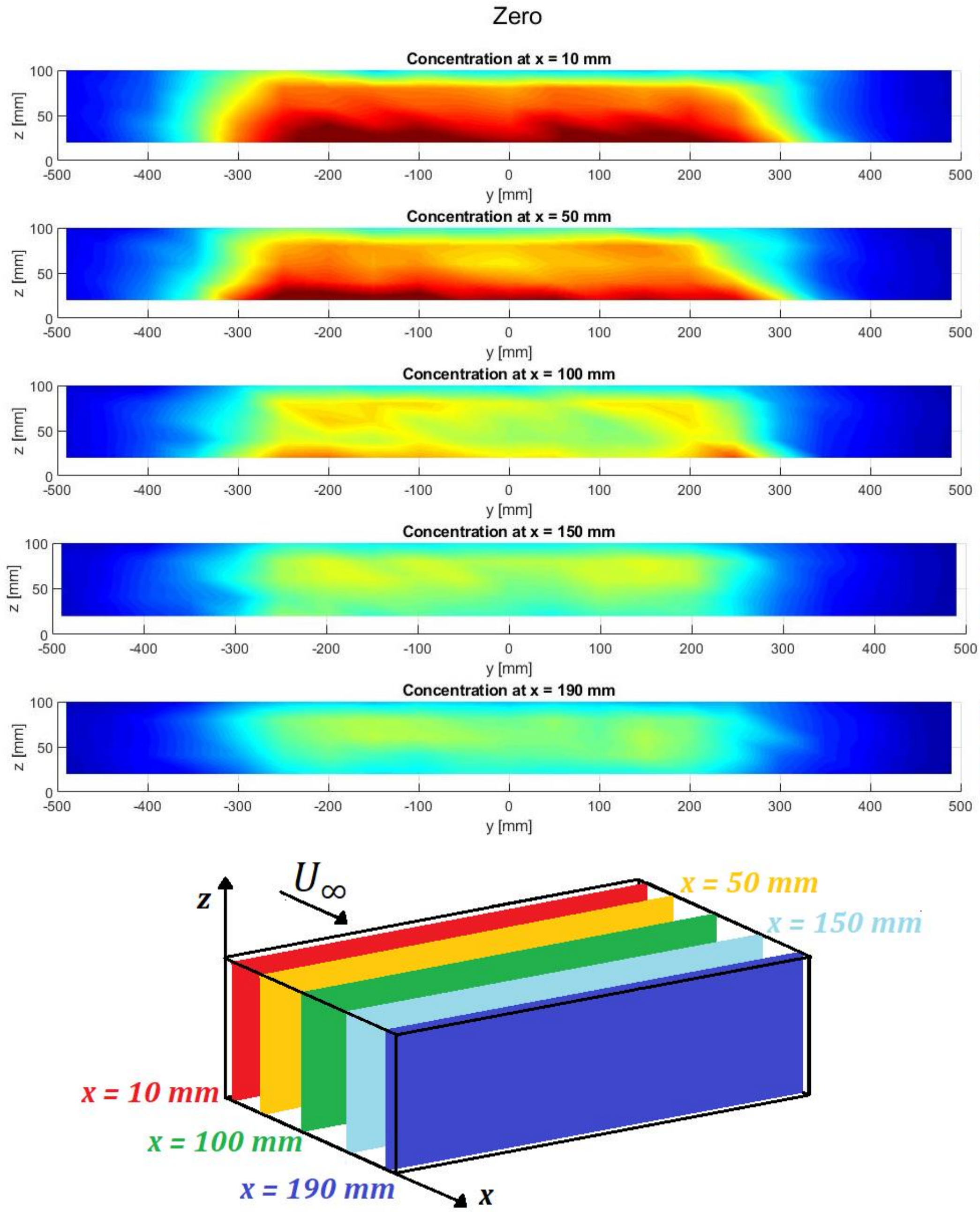


*Figure 2.3.1– Concentration field at different sections along x direction, i.e., wind direction for the "zero" configuration. From top to bottom the five sections at increasing distance from the upwind wall. The sections are represented in the sketch at the bottom of the picture.*

On the other hand, in the "full" configuration, the trees are really closed between each other, and this could reduce the degrees of freedom of the flow, producing a more organised structure. Finally, in the sections furthest away from the upwind wall, the “half” configuration shows a higher concentration between the peaks with respect to the “full” configuration. This suggests a stronger homogenization effect in the “half” configuration suggesting in turn a more developed turbulence.

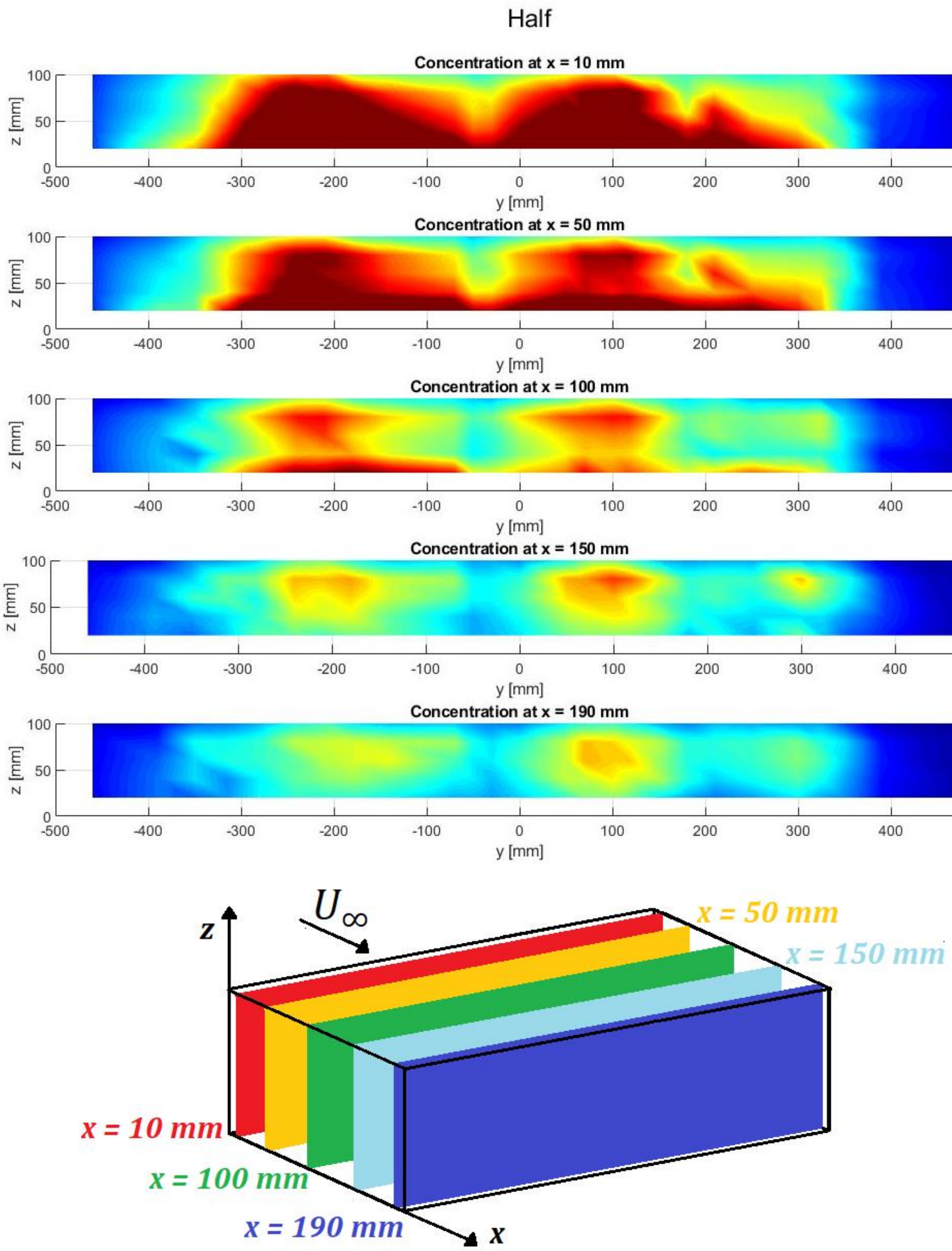


*Figure 2.3.2– Concentration field at different sections along x direction, i.e., wind direction for the “half” configuration. From top to bottom the five sections at increasing distance from the upwind wall. The sections are represented in the sketch at the bottom of the picture.*

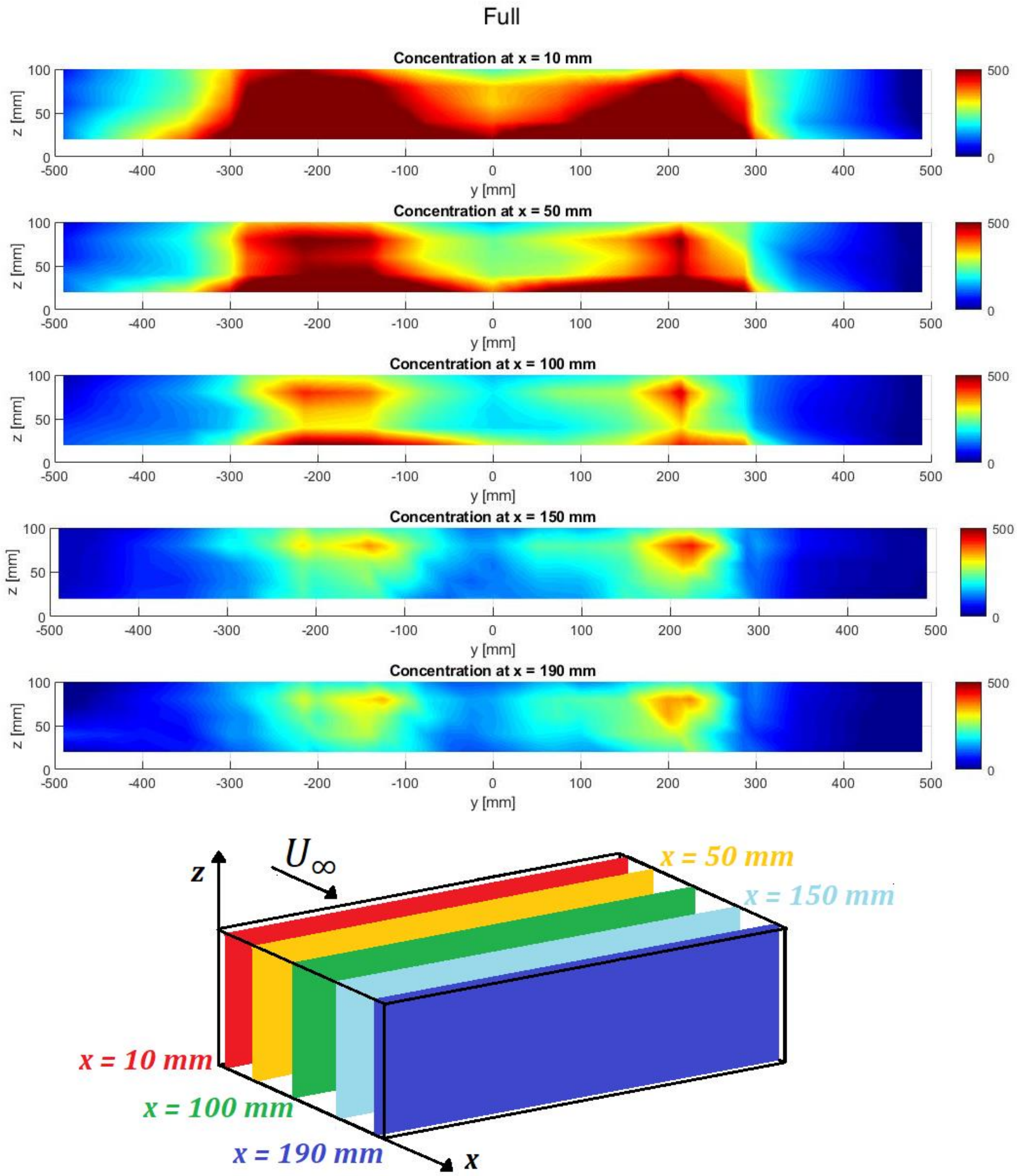


***Figure 2.3.3*** *– Concentration field at different sections along x direction, i.e., wind direction for the "full" configuration. From top to bottom the five sections at increasing distance from the upwind wall. The sections are represented in the sketch at the bottom of the picture.*

*Figure 2.3.4* shows the profiles of the concentration field at different sections along x direction, i.e., the wind direction, for the three configurations considered. The profiles in three sections keep more or less the same shape but as already seen in the previous pictures, the concentration values decrease with the distance from the upwind wall. These profiles show in a clearer way the peaks of concentration in the configurations with the trees and the homogeneity in the “zero” configuration. It is also easy to see how the “half” configuration results to be less structured with respect to the “full” configuration.

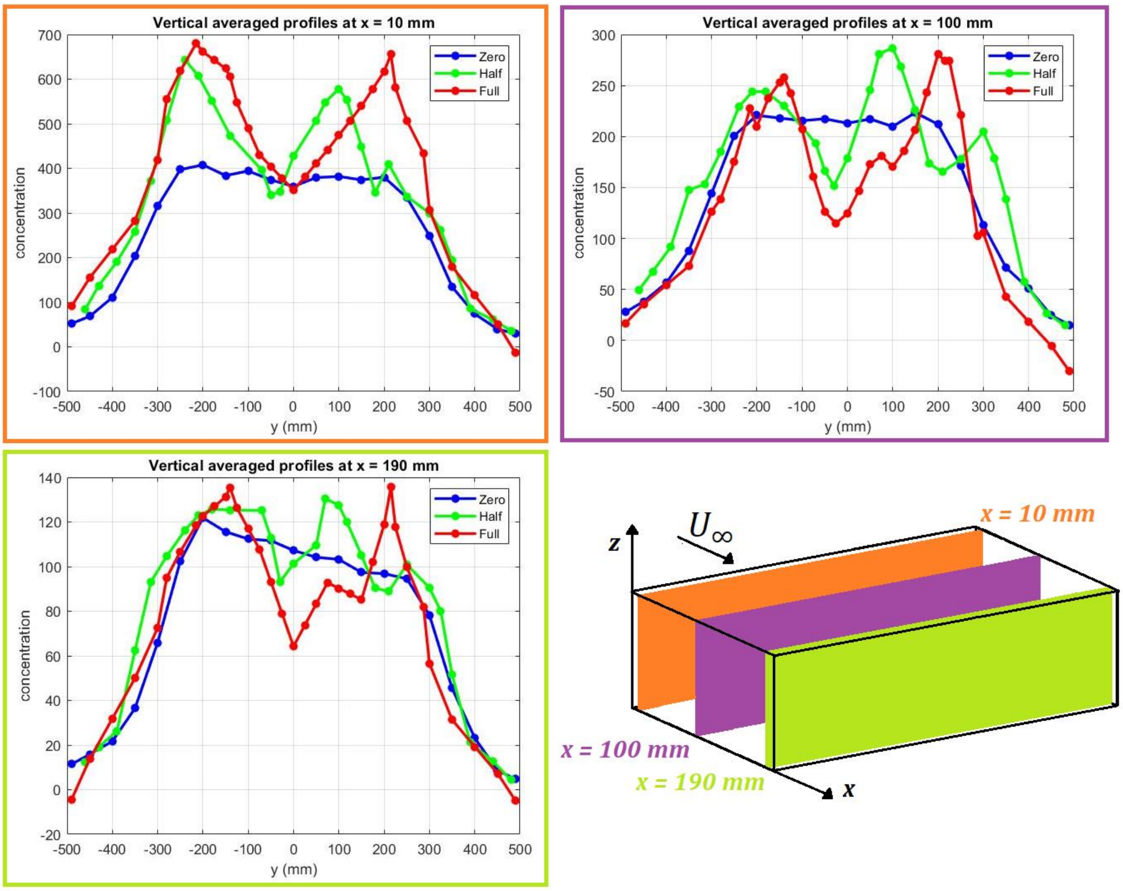


*Figure 2.3.4– Profiles of concentration field at different sections along x direction, i.e., wind direction for the three configurations considered. The sections are represented in the sketch at the bottom right corner of the picture. The profiles are averaged along z direction, i.e., vertical averaged.*

Finally, *Figure 2.3.5* shows the concentration field at different sections along y direction. This picture shows how in the “zero” configuration the concentration field seems to be nearly two-dimensional. In fact, moving along y direction, no significant changes in the concentration field structure and values are present. This aspect changes when the trees are present. In fact, in the “half” and “full” configurations the concentration field is strongly three-dimensional. In particular, in the “full” configuration, a more well organised structure in the concentration field is clearly visible. This could be seen in the structure of the sections of the concentration field when moving along y direction. These sections always show an accumulation of pollutant near the upwind wall of the cavity. Instead, in the "half" configuration, it is possible to find sections whit different structures when moving along y direction.

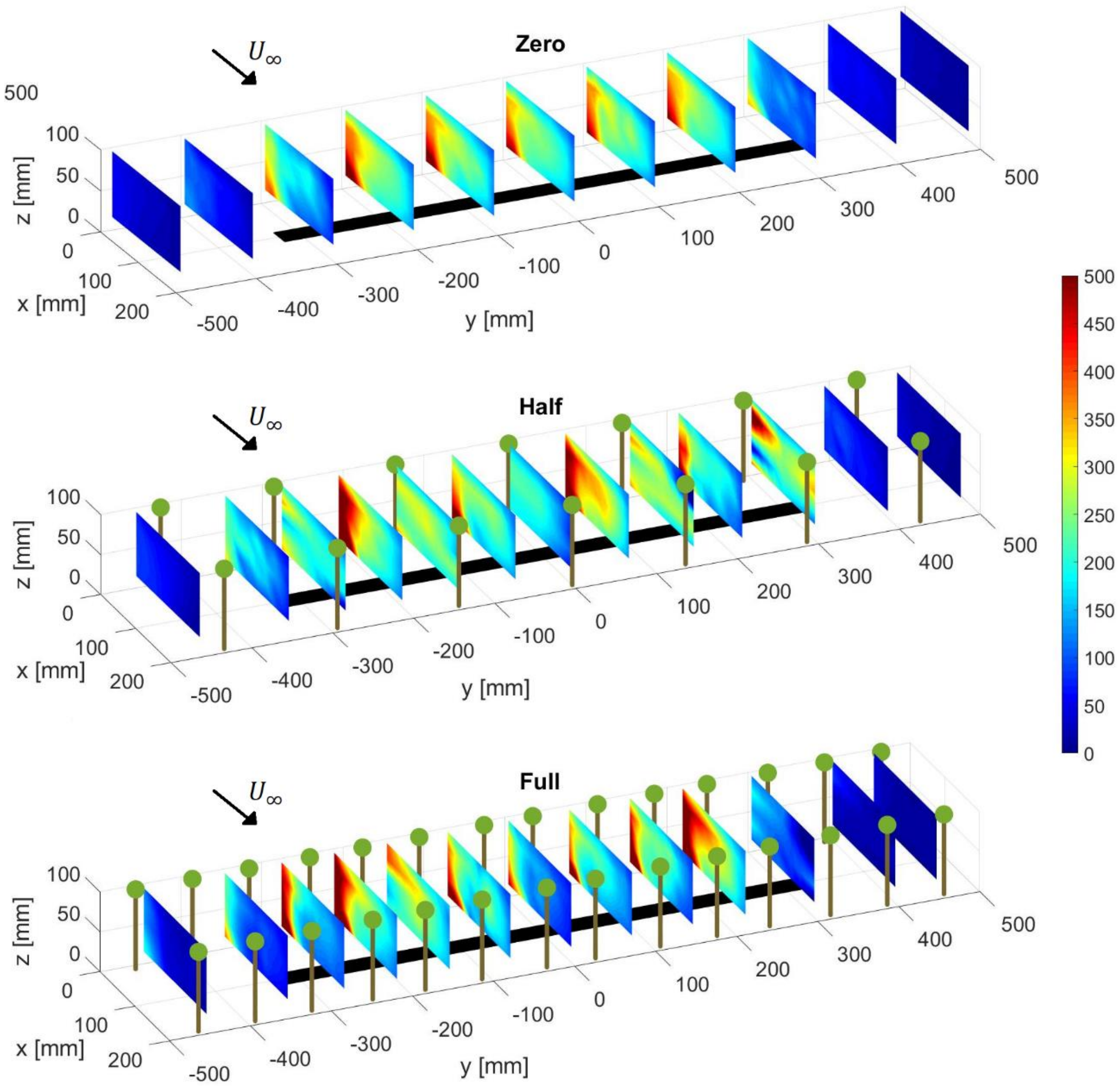


*Figure 2.3.5– Concentration field at different sections along y direction. From top to bottom the three configurations considered. The black bar on the ground represents the ethane source, the green dots represent the crowns of the trees, and the brown lines represent the trunks.*

## 2.3.2 Vertical exchange velocity

The vertical exchange velocity between the street canyon and the external flow has been computed to evaluate the effect of the trees on the ventilation and on the dispersion of the pollutants in the canyon. This has been made possible by the fact that, in this study, the canyon is closed at the sides so is like a box where the quantity of ethane emitted by the source can only get out from the top of the cavity. This information can be mathematically written with the relation

$$Q_{et} = \langle c \rangle U_d L_{cav} W_{cav}, \tag{2.2}$$

where $\langle c \rangle$ is the concentration averaged overall the cavity, $U_d$ is the vertical exchange velocity to estimate, $L_{cav}$ the length of the cavity and $W_{cav}$ the width of the cavity.

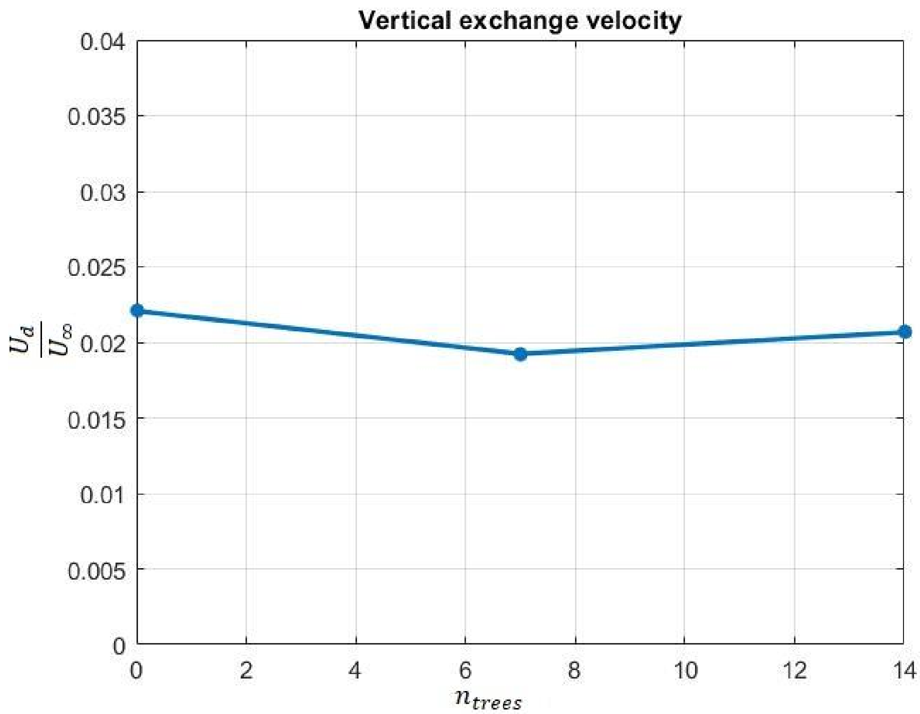


***Figure 2.3.6***– *Vertical exchange velocity computed for the three different configurations. The velocity is normalized with respect to the horizontal velocity at the top of the boundary layer, i.e., $U_\infty$. The number of trees 0, 7 and 14 stay for "zero", "half" and "full" configurations respectively.*

*Figure 2.3.6* shows the obtained values for the vertical exchange velocity for the three configurations considered, i.e., 0, 7 and 14 trees on each row. It is easy to notice that no significant changes are present when changing the number of trees. This suggests that the presence of trees does not affect the ventilation in the canyon. This result might seem to disagree with the previous one, i.e., the fact that the concentration field loses its two-dimensionality when adding the trees. Actually, it is important to notice that this result refers to a space dependent concentration, instead, the vertical exchange velocity uses the information on the averaged concentration field. This ends up in having a strong effect of the trees on the concentration field but not on the mean concentration field. In other terms, the trees influence the flow field bringing a different distribution of the pollutant in the canyon but do not affect the global quantity of pollutant in the canyon.

# 3. Numerical investigation

In this second part of the work results from RANS (Reynolds-Averaged Navier-Stokes) simulations will be presented. Numerical simulations in the field of fluid mechanics identify the so-called Computational Fluid Dynamics (CFD). The aim of CFD is the resolution of Navier-Stokes equations using space-time discretization. Nowadays, there are three fundamental approaches to this purpose:

- *RANS (Reynolds-Averaged Navier-Stokes)* simulations are based on the idea of Reynolds decomposition which consists in writing each variable in Navier-Stokes (NS) equations as the sum of a time-averaged part and a fluctuating part. After this procedure the decomposed variables are substituted into time-averaged NS equations so that one gets the equations for the mean flow in which a term owning the fluctuating velocity components appears. This term is referred to as Reynolds stress tensor and it needs a mathematical modelling (e.g., $k - \varepsilon$, $k - \omega$).
- *LES (Large eddy simulation)* resolves the largest length scales of turbulence and model the smallest ones. This approach is made possible observing that most of the kinetic energy is contained in the largest eddies. The identification of the scales range to simulate is processed by means of a low-pass filtering operation. As RANS simulations, LES need mathematical modelling of the smallest scales. These models are referred to as sub-grid scale models.
- *DNS (Direct numerical simulation)* resolves the entire range of turbulent length scales consequently there is no need for turbulence models. This approach is extremely expensive and intractable for flow with complex geometries. Anyway, these simulations applied on simpler cases allow a better understanding of the physics of turbulence.

It is useful to underline that RANS simulations, due to the inherent constraints of the RANS approach, provide only a qualitative behaviour of the concentration field, the description of turbulent structures being neglected. Therefore, it would certainly be interesting to carry out LES or DNS in this study. On the other hand, a DNS in this case might not be easily achievable, due to the complex geometry and to the significantly small turbulence scales possibly resulting from the presence of trees. The main goal of this second part of the work has been to attempt a first simple numerical approach to the study. Therefore, two dimensional RANS simulations have been carried out.
In the following, some general notions will be provided to better understand how a RANS simulation works.

## 3.1 RANS equations

In this paragraph RANS equations from the instantaneous NS equations will be derived to describe some of the most well-known turbulence models. The analysis will be done for an incompressible Newtonian fluid so that NS equations in tensor notation are written as

$$\frac{\partial u_i}{\partial x_i} = 0$$
$$\frac{\partial u_i}{\partial t} + u_j \frac{\partial u_i}{\partial x_j} = f_i - \frac{1}{\rho}\frac{\partial p}{\partial x_i} + \nu \frac{\partial^2 u_i}{\partial x_j^2} \tag{3.1}$$

where $u$ is the velocity vector, $p$ the pressure, $f$ the vector of the external forces, $\rho$ the density and $\nu$ the kinematic viscosity.
The first step is to use Reynolds decomposition which refers to the separation of each variable into a time-averaged component (denoted with the overbar) and a fluctuating component (denoted with the prime). The Reynolds decompositions for $u$, $p$ and $f$ respectively are written as

$$
\begin{aligned}
u(\boldsymbol{x},t) &= \bar{u}(\boldsymbol{x}) + u'(\boldsymbol{x},t) \\
p(\boldsymbol{x},t) &= \bar{p}(\boldsymbol{x}) + p'(\boldsymbol{x},t) \\
f(\boldsymbol{x},t) &= \bar{f}(\boldsymbol{x}) + f'(\boldsymbol{x},t)
\end{aligned}
\tag{3.2}
$$

where $\boldsymbol{x} = (x, y, z)$ is the position vector and the time-average operator $A$ applied on a general function $a(\boldsymbol{x},t)$ is defined as

$$
A\big(a(\boldsymbol{x},t)\big) = \bar{a}(\boldsymbol{x}) = \lim_{T\to\infty} \frac{1}{T}\int_{t_0}^{t_0+T} a(\boldsymbol{x},t)\,dt. \tag{3.3}
$$

Taken two general functions $a(\boldsymbol{x},t)$ and $b(\boldsymbol{x},t)$, the time-average operator has the following properties:

$$
\begin{gathered}
A\big(a(\boldsymbol{x},t) + b(\boldsymbol{x},t)\big) = A\big(a(\boldsymbol{x},t)\big) + A\big(b(\boldsymbol{x},t)\big) \\
A\Big(A\big(a(\boldsymbol{x},t)\big)\Big) = A\big(a(\boldsymbol{x},t)\big) \\
A\big(a'(\boldsymbol{x},t)\big) = 0.
\end{gathered}
\tag{3.4}
$$

Substituting the Reynolds-decomposed variables in (3.1) and applying a time-average operation all over the equations we obtain

$$
\begin{gathered}
\overline{\frac{\partial(\bar{u}_i + u_i')}{\partial x_i}} = 0 \\
\overline{\frac{\partial(\bar{u}_i + u_i')}{\partial t}} + \overline{(\bar{u}_j + u_j')\frac{\partial(\bar{u}_i + u_i')}{\partial x_j}} = \overline{(\bar{f}_i + f_i')} - \frac{1}{\rho}\overline{\frac{\partial(\bar{p} + p')}{\partial x_i}} + \nu\overline{\frac{\partial^2(\bar{u}_i + u_i')}{\partial x_j^2}}.
\end{gathered}
\tag{3.5}
$$

Using the time-averaged operator properties and observing that

$$
\frac{\partial \bar{u}_i}{\partial t} = 0 \tag{3.6}
$$

we get

$$\frac{\partial \bar{u}_i}{\partial x_i} = 0$$

$$\overline{u}_j \frac{\partial \overline{u}_i}{\partial x_j} = \overline{f}_i - \frac{1}{\rho}\frac{\partial \overline{p}}{\partial x_i} + \nu \frac{\partial^2 \overline{u}_i}{\partial x_j^2} - \frac{\partial \overline{u_i' u_j'}}{\partial x_j} \qquad (3.7)$$

where the quantity $\overline{u_i' u_j'}$ is the only one still containing information about turbulent fluctuations. Multiplying by $\rho$ the second equation we can get the term $\rho\overline{u_i' u_j'}$ which is referred to as Reynolds stress tensor. The starting point of RANS simulations is the mathematical modelling of Reynolds stress tensor in terms of the mean flow in order to solve the approximate deriving equations (the so-called *closure problem*). In this way, a RANS simulation is not representative of any turbulence scale but provides information about the mean flow and the effect that turbulence has on it.

### 3.1.1 Solving RANS equations: eddy viscosity models

Several models are available to approximate Reynolds stress tensor. An important class of models is that of the so-called eddy viscosity models (EVM) (Wilcox D.C., 1998). These models are based on the concept of eddy viscosity introduced by Joseph Valentin Boussinesq. The idea is to model Reynolds stress tensor using the Boussinesq hypothesis

$$-\overline{u_i' u_j'} = \nu_t \left( \frac{\partial \overline{u_i}}{\partial x_j} + \frac{\partial \overline{u_j}}{\partial x_i} \right) - \frac{2}{3} k \delta_{ij} \qquad (3.8)$$

where $k$ is the turbulent kinetic energy (TKE) defined as

$$k = \frac{1}{2}\overline{u_i' u_i'} \qquad (3.9)$$

and $\delta_{ij}$ is the Kronecker delta. The quantity $\nu_t$ is the eddy viscosity and it can be simply a constant or, more generally, a function of variables related to turbulence. Depending on the way $\nu_t$ is modelled, we get to different models. In the following $k-\varepsilon$, $k-\omega$ and $SST$ ($Shear\ Stress\ Transport$) $k-\omega$ models will be described. The models take their names from the choice of the variables used to define the eddy viscosity. For $\boldsymbol{k-\varepsilon}$ **model**,

$$\nu_t = C_\mu \frac{k^2}{\varepsilon} \tag{3.10}$$

where $C_\mu$ is a constant experimentally obtainable, $k$ is the TKE and $\varepsilon$ defined as

$$\varepsilon = \nu \overline{\frac{\partial u_i'}{\partial x_j}\frac{\partial u_i'}{\partial x_j}} \tag{3.11}$$

is the rate of dissipation of TKE. The model is completed writing two further equations, for $k$ and $\varepsilon$ respectively. The equation for $k$ can be derived subtracting NS equations from RANS equations, multiplying by $u_i'$ and applying a time-average operation. Doing that, we obtain a new equation in which terms depending on turbulent fluctuations appear. These terms need to be modelled. To this purpose two hypothesis are used, the aforementioned Boussinesq hypothesis and the gradient diffusion hypothesis which assumes $k$ to be transported from high value region to low value region of $k$. Assuming that, the obtained equation for $k$ is

$$\frac{\partial k}{\partial t} + \frac{\partial \overline{u_i} k}{\partial x_i} = \frac{\partial}{\partial x_j}\left(\left(\frac{\nu_t}{\sigma_k} + \nu\right)\frac{\partial k}{\partial x_j}\right) - \nu_t\left(\frac{\partial \overline{u_i}}{\partial x_j} + \frac{\partial \overline{u_j}}{\partial x_i}\right)\frac{\partial \overline{u_i}}{\partial x_j} - \varepsilon. \tag{3.12}$$

where $\sigma_k$ is an experimentally obtainable constant. The equation for $\varepsilon$ could also be derived from NS and RANS equations but that leads to a much more complicated equation in which the terms containing turbulent fluctuations have a too uncertain modelling. For this reason, writing for $\varepsilon$ an equation analogous to $k$ equation is preferable. Since we have

$$[k] = \frac{m^2}{s^2}, \qquad [\varepsilon] = \frac{m^2}{s^3} \tag{3.13}$$

we need to divide the last two terms in $k$ equation by a quantity that is dimensionally equivalent to time to get a dimensionally correct equation for $\varepsilon$. To that purpose the turbulent characteristic time $k/\varepsilon$ is chosen. So that, we obtain

$$\frac{\partial \varepsilon}{\partial t} + \frac{\partial \overline{u_i}\varepsilon}{\partial x_i} = \frac{\partial}{\partial x_j}\left(\left(\frac{\nu_t}{\sigma_\varepsilon} + \nu\right)\frac{\partial \varepsilon}{\partial x_j}\right) - \frac{\varepsilon}{k} C_{1\varepsilon}\nu_t \left(\frac{\partial \overline{u_i}}{\partial x_j} + \frac{\partial \overline{u_j}}{\partial x_i}\right)\frac{\partial \overline{u_i}}{\partial x_j} - C_{2\varepsilon}\frac{\varepsilon^2}{k} \tag{3.14}$$

where $\sigma_\varepsilon$, $C_{1\varepsilon}$ and $C_{2\varepsilon}$ are constants that can be obtained experimentally.
Another available model in literature is the $\boldsymbol{k - \omega}$ **model**, in which

$$\nu_t = \frac{k}{\omega}, \tag{3.15}$$

where $\omega$ rapresents the specific rate of dissipation of TKE into internal thermal energy and is assumed to be proportional to specific dissipation $\varepsilon/k$ through a proportionality constant $\beta^*$. The model consists of two equations for $k$ and $\omega$ respectively. The equation for $k$ is the same of $k - \varepsilon$ model and the equation for $\omega$ is derived from $k$ equation using the aforementioned assumption on $\omega$. The final equations are written as

$$\frac{\partial k}{\partial t} + \frac{\partial \overline{u_i}k}{\partial x_i} = \frac{\partial}{\partial x_j}\left(\left(\frac{\nu_t}{\sigma_k^\omega} + \nu\right)\frac{\partial k}{\partial x_j}\right) - \nu_t \left(\frac{\partial \overline{u_i}}{\partial x_j} + \frac{\partial \overline{u_j}}{\partial x_i}\right)\frac{\partial \overline{u_i}}{\partial x_j} - \beta^*\omega k$$
$$\frac{\partial \omega}{\partial t} + \frac{\partial \overline{u_i}\omega}{\partial x_i} = \frac{\partial}{\partial x_j}\left(\left(\frac{\nu_t}{\sigma_\omega} + \nu\right)\frac{\partial \omega}{\partial x_j}\right) - \frac{\omega}{k} C_{1\omega}\nu_t \left(\frac{\partial \overline{u_i}}{\partial x_j} + \frac{\partial \overline{u_j}}{\partial x_i}\right)\frac{\partial \overline{u_i}}{\partial x_j} - C_{2\omega}\omega^2 \tag{3.16}$$

where $\sigma_k^\omega$, $\sigma_\omega$, $C_{1\omega}$ and $C_{2\omega}$ are constants that can be obtained experimentally.
It is well known that $k-\varepsilon$ model doesn't show a good sensibility to flows with adverse pressure gradient. Another weakness of this model is in general related to wall-bounded flows. Nevertheless, it shows a pretty good accuracy in predicting flow behaviour in regions away from the wall. The $k-\omega$ model is instead well suited for simulating flow in the viscous sub-layer i.e., the closest layer to the wall. For this reason, the best compromise lies in ***SST*** $\boldsymbol{k-\omega}$ **model**. This is a hybrid model combining $k-\omega$ and $k-\varepsilon$ models where a blending function activates $k-\omega$ model near the wall and $k-\varepsilon$ model in the free stream. The model is based on the correction of turbulent production term in $k$ and $\varepsilon$ equations, avoiding a build-up of excessive TKE near stagnation points, characterizing $k-\varepsilon$ model.
These considerations underlie the choice to use *SST* $k-\omega$ model in Ansys Fluent.

## 3.2 2D RANS simulations

In this paragraph, setup and results of the carried-out simulations will be presented. The results in *Chapter 2* suggest the possibility to do a two-dimensional study for the configuration without trees, since the pollutant concentration field is a nearly two-dimensional field.

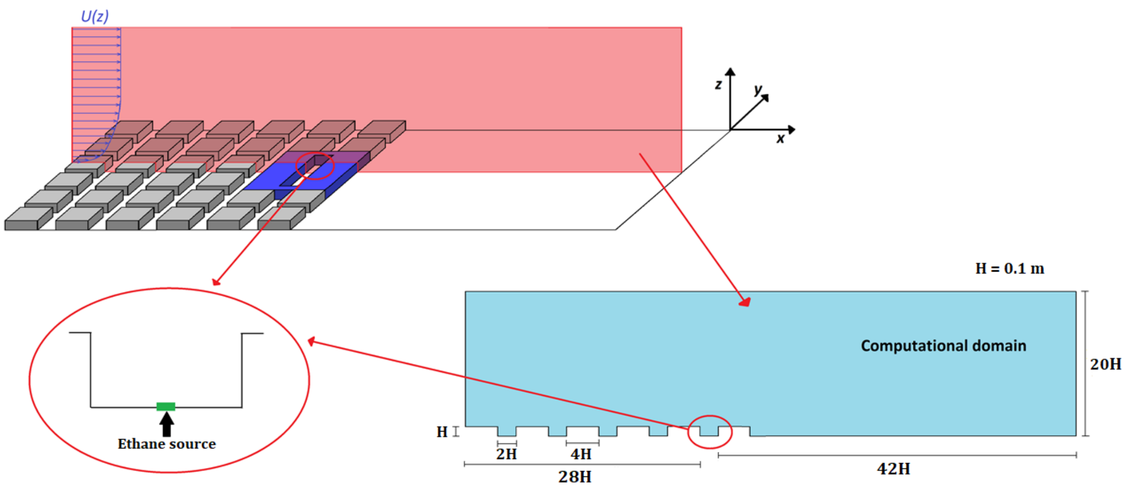


***Figure 3.2.1*** *– Sketch of computational domain. In the upper part, a three-dimensional sketch reproducing the experiment. In the lower part the two-dimensional domain used for simulations (right) and a section of the canyon (left).*

A two-dimensional study for a configuration with trees has been also carried out. In this last case, two squared boxes are added in the geometry to simulate the presence of trees, as shown in *Figure 3.2.2.*

It is important to notice that the results presented in the first part of this work do not justify a two-dimensional simulation when trees are present, since the concentration field in all the analysed configurations with trees in strongly three-dimensional. However, it could be interesting to find a qualitative estimation of the error committed with a two-dimensional approximation. In *Figure 3.2.1* a sketch of the computational domain is showed. As shown in *Figure 3.2.2*, the two squared boxes aim to reproduce, using a two-dimensional analysis, the three-dimensional case in which two continuous rows of trees are present. Finally, can be assumed that this last configuration approximates the "full configuration", in order to compare numerical and experimental results.

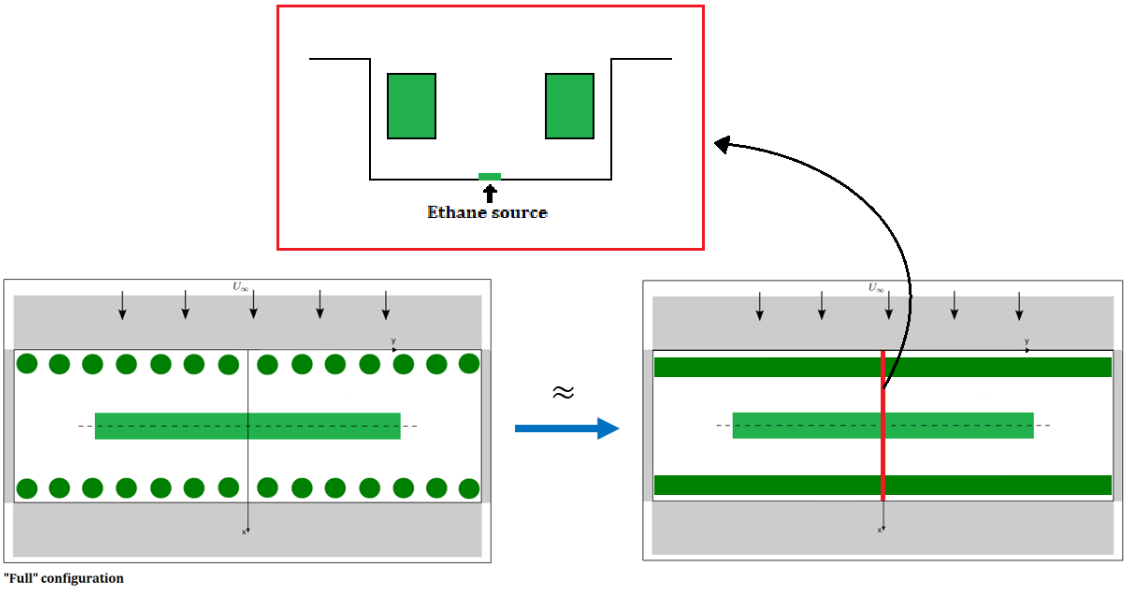


***Figure 3.2.2**– Sketch of geometry in simulation with trees (up) and assumption done on the distribution of the trees (down) i.e., the full configuration can be approximated with a configuration with two continuous rows of trees.*

### 3.2.1 Mesh

*Figure 3.2.3* shows the mesh used in all the simulations. The mesh consists of quadrangular cells, properly intensified near the walls at the bottom part of the domain and around the tree-zone, i.e., in the zones in which a higher resolution is needed.

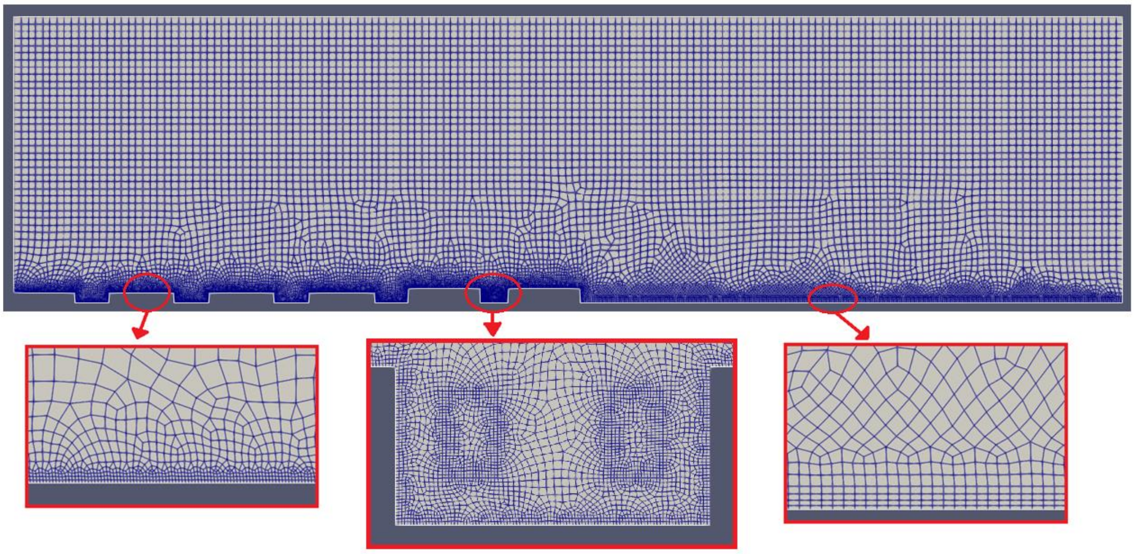

***Figure 3.2.3*** – *Defined mesh. Details of the refinement near the walls and along the perimeter of the trees.*

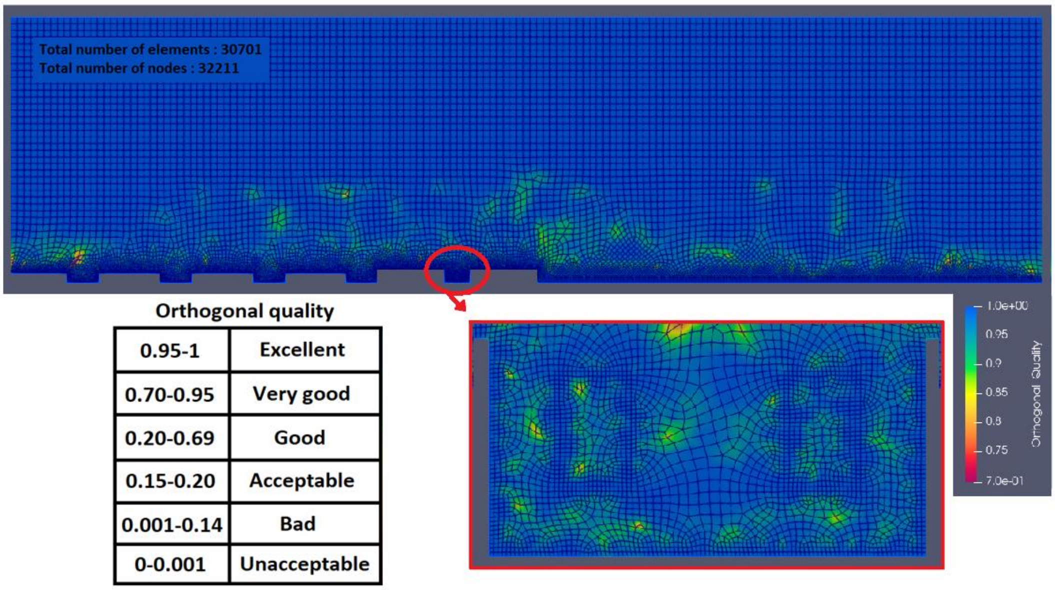


**Orthogonal quality**

| | |
|---|---|
| 0.95-1 | Excellent |
| 0.70-0.95 | Very good |
| 0.20-0.69 | Good |
| 0.15-0.20 | Acceptable |
| 0.001-0.14 | Bad |
| 0-0.001 | Unacceptable |

***Figure 3.2.4*** – *Orthogonal quality of the mesh. The table shows the different levels of quality using a range of colours: from green to blue the mesh is considered to have a good to excellent orthogonal quality.*

One of the important features to define a good mesh is the orthogonality property. This property relates to the angles between adjacent cells edges. The closer the cells angles are to right angles, the higher the orthogonality quality is.
*Figure 3.2.4* shows mesh quality measured respect to this property and a table of quality levels. It is easily observable that the used mesh has very good to excellent orthogonal quality. A mesh sensitivity test has been done halving the cell edge length along the walls at the bottom part of the domain and along the perimeter of the squared boxes, starting from a significantly coarse mesh to a mesh doubly fine with respect to the one presented. The simulation results showed insensitivity to subsequent improvement of the mesh presented here (see *Figure 3.3.17*).

## 3.2.2 Initial and boundary conditions

*Figure 3.2.5* shows a subdivision of the boundaries of the computational domain, highlighting, with different colours, the edges which need different boundary conditions.

***Figure 3.2.5*** *– Computation domain with highlighted boundaries: top wall (red), down wall (yellow), inlet (green), outlet (blue), ethane source (black).*

For the top wall in red, a symmetry boundary condition has been prescribed. This condition in Ansys Fluent assumes zero normal velocity end zero normal gradients of all the variables at the considered edge. Therefore, there is no convective or diffusive flux across the top wall. For the down wall in yellow, a no-slip condition has been prescribed. This means that horizontal velocity on this edge is zero. For the inlet in green, a velocity-inlet boundary condition is used. This condition allows to assign profiles for velocity and turbulence parameters to the inlet flow. To this purpose, experimental fitted data have been used. In particular, the vertical velocity profile experimentally obtained in proximity of the red point in *Figure 3.2.6* has been used at the inlet to get a faster convergence. Similarly, knowing velocity components, TKE has been computed to be used at the inlet. For the outlet in blue, a pressure outlet boundary condition has been used. This choice permits to define gauge pressure at the outlet, i.e., the pressure measured relative to the ambient atmospheric pressure. In this contest gauge pressure has been set equal to zero. Finally, for the ethane source in black, a velocity-inlet boundary condition has been assigned. The value of the inlet velocity of ethane-air mixture flow has been computed using the relation between velocity and flow rate knowing the real flow rate in the experiments.

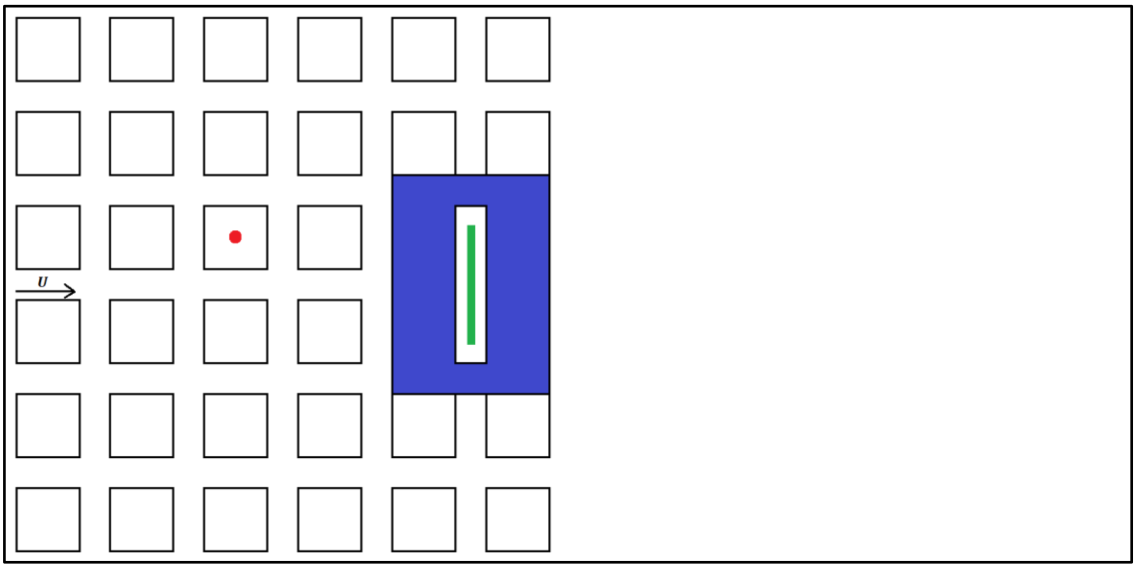


***Figure 3.2.6*** *– Top view of the domain. The red point identifies the position at which horizontal velocity components have been measured.*

### 3.2.3 Model parameters

The carried-out simulations consider two parameters: roughness height $R_h$ and turbulent Schmidt number $S_{C_t}$. The latter is defined as

$$S_{C_t} = \frac{\nu_t}{K} \tag{3.17}$$

where $\nu_t$ is the eddy viscosity and $K$ the eddy diffusivity. Eddy diffusivity relates to turbulent mixing. Increasing values of $K$ lead to increasing mixing and therefore increasing rate of mass, momentum and energy transport. For $S_{C_t}$, Ansys Fluent default value $S_{C_t} = 0.7$ has been considered as a starting value, followed by $S_{C_t} = 0.5$ and $S_{C_t} = 0.9$. The values for $R_h$ instead, have been chosen starting from the experimental obtained value i.e., $R_h = 0.023$, and considering other two values, a higher one $R_h = 0.03$ and a lower one $R_h = 0.015$.

| | | Base case | | | | | | | |
|---|---|---|---|---|---|---|---|---|---|
| $S_{C_t}$ | 0.5 | 0.7 | 0.9 | 0.5 | 0.7 | 0.9 | 0.5 | 0.7 | 0.9 |
| $R_h$ | 0.023 | 0.023 | 0.023 | 0.015 | 0.015 | 0.015 | 0.03 | 0.03 | 0.03 |

***Table 3.2.1*** *– On the columns the nine cases analysed. Turbulent Schmidt number in the first row and roughness height in the second one.*

All the possible combinations of values lead to nine cases, summarized in *Table 3.2.1.*

# 3.3 Results

In the following, results obtained from the carried-out simulations for the configurations with and without trees will be presented.

## 3.3.1 Configuration without trees

In this paragraph, results obtained from simulations for the configuration without trees will be shown. A preliminary check of the flow approaching the cavity has been done computing the horizontal velocity component profile and the TKE profile on the top of the building just before the cavity. The obtained profiles are shown in *Figure 3.3.1.* It is immediate to notice that the velocity profile results in a strong agreement with the expected profile, i.e., the experimental obtained profile. On the other hand, the picture shows as the simulations overestimate the values of TKE, especially near the wall. Furthermore, it is possible to notice that, increasing roughness height, TKE values increase. This is not surprising since roughness height is related to wall properties and higher values of roughness promotes the triggering of turbulence and so of TKE.

In *Figure 3.3.2* results of the concentration field for all the analysed cases are reported and compared to the experimental one. All the simulated values have been made dimensionless using the relation

$$c_{num}{}^{*} = \frac{c_{num}\, U_{2H} H}{c_s u_s L_w}, \tag{3.18}$$

where $c_{num}$ is the numerical obtained concentration, $H$ the buildings height, $U_{2H}$ the simulated horizontal velocity component value at $z = 2H$, $c_s$ the mass fraction of ethane in the ethane-air mixture released from the source, $u_s$ the velocity assigned to the flux at the source as inlet condition and $L_w$ the width of the source. In a similar way, the experimental values have been made dimensionless using the relation

$$c_{exp}{}^{*} = \frac{c_{exp} U_{2H} H}{Q_{et}}, \tag{3.19}$$

where $c_{exp}$ is the experimental obtained concentration, $U_{2H}$ the experimental horizontal velocity component value at $z = 2H$, $H$ the buildings height and $Q_{et}$ the ethane quantity released from source in the experiments.

Results show that low Schmidt number tend to underestimate the concentration in the right part of the cavity, instead high Schmidt number tends to overestimate the concentration all over the cavity. Given the definition of the Schmidt number, it is expected that increasing Schmidt number, turbulent diffusivity decreases i.e., lower values of Schmidt number help increasing turbulent diffusivity thus counteracting the accumulation of ethane in the left part of the cavity.

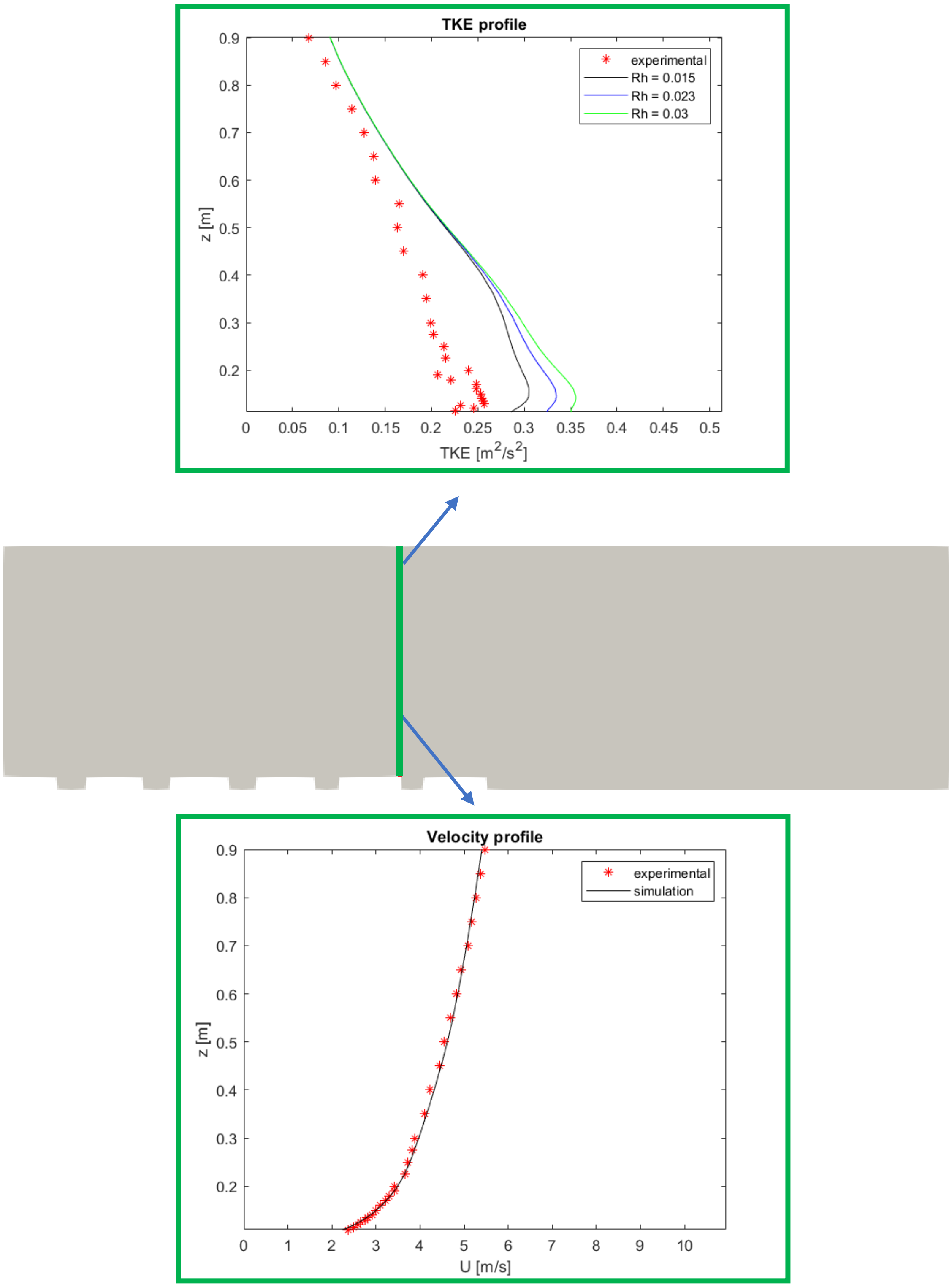


***Figure 3.3.1–*** *TKE and horizontal velocity component profiles on the top of the building before entering the cavity. TKE profiles for the three roughness height values used are shown and compared with the experimental profile. The image shows as TKE increases with increasing roughness height. It is easy to notice that simulations overestimate TKE near the wall. Horizontal velocity component profile is instead in strong agreement with the experimental data.*

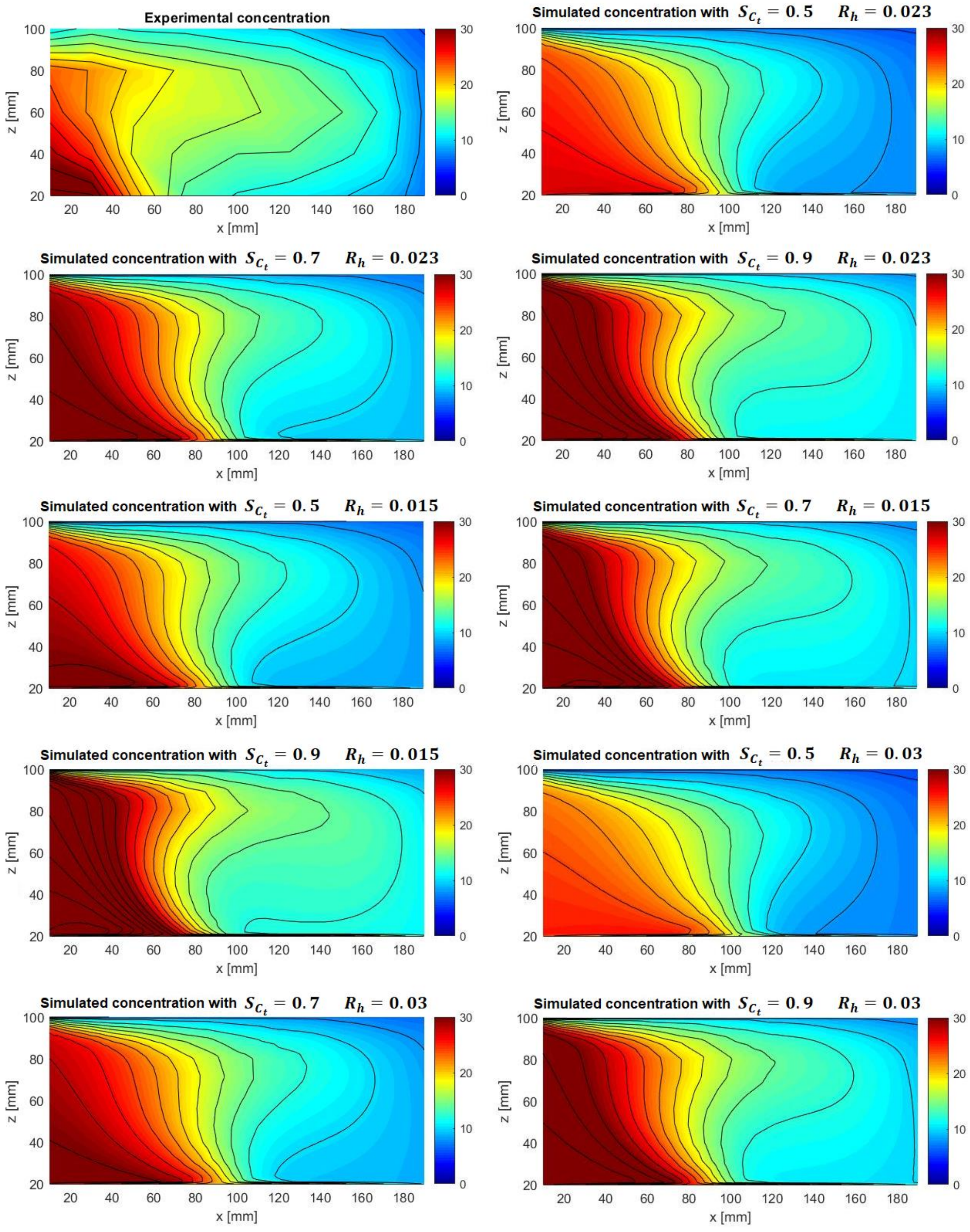


*Figure 3.3.2– Concentration field with contour lines obtained in all the carried-out simulations changing roughness height and Schmidt number. The first image at the top left shows the experimental concentration field.*

To better analyse this aspect, *Figure 3.3.3* shows how the concentration field changes increasing Schmidt number with fixed roughness height. The concentration values in each case have been rescaled dividing by the mean concentration value.

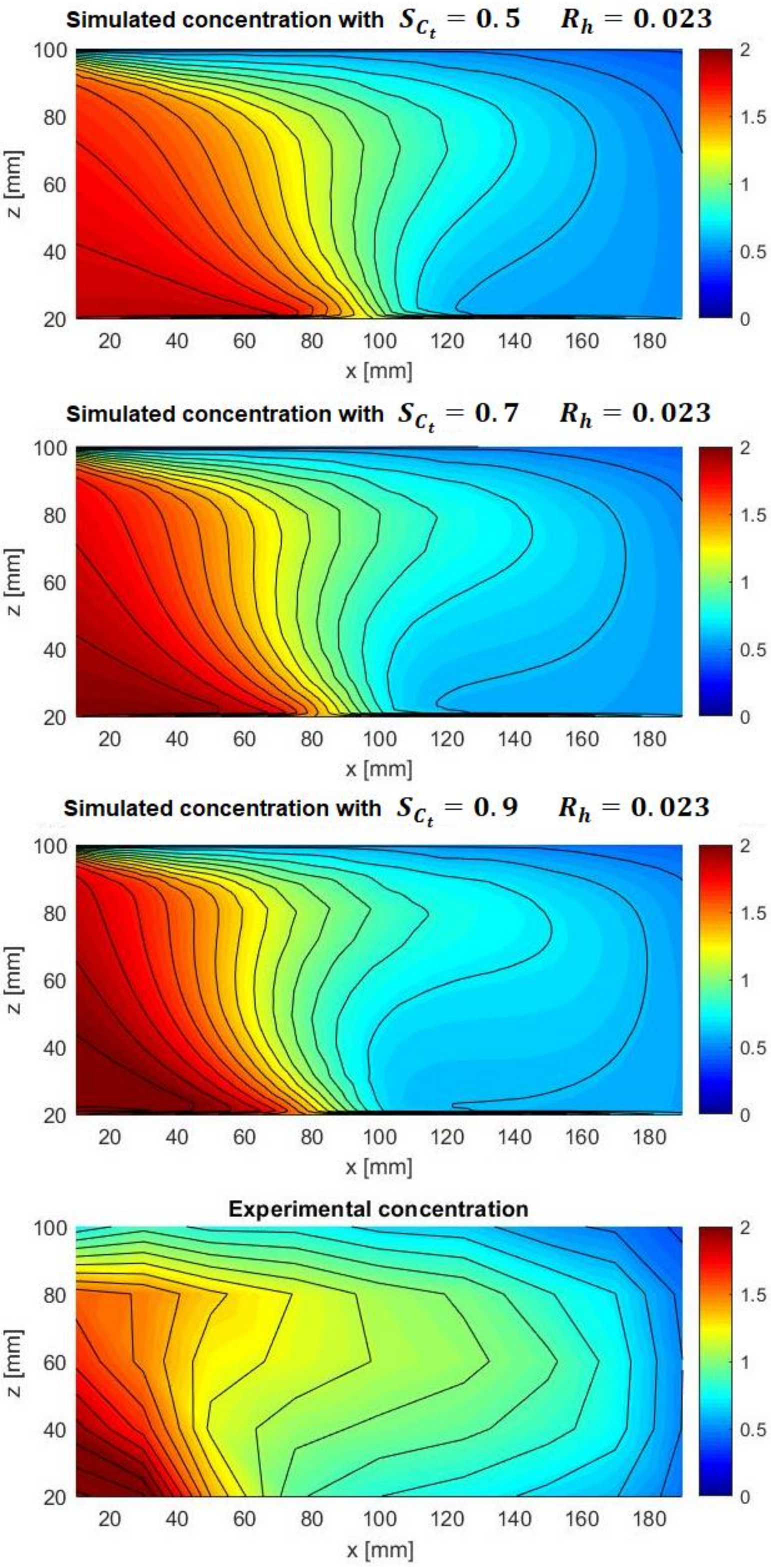


*Figure 3.3.3– From the top to bottom, concentration field obtained increasing Schmidt number with fixed roughness height $R_h = 0.023$. Experimental concentration field at the bottom. The fixed roughness height value is the one experimentally obtained i.e., the value of the base case highlighted in Figure 3.2.7.*

This permits to consider the total quantity of ethane in the cavity in order to better appreciate the differences among the three cases. As expected, the contour lines show that with higher values of Schmidt number, the ethane tends to accumulate in the left part of the cavity.

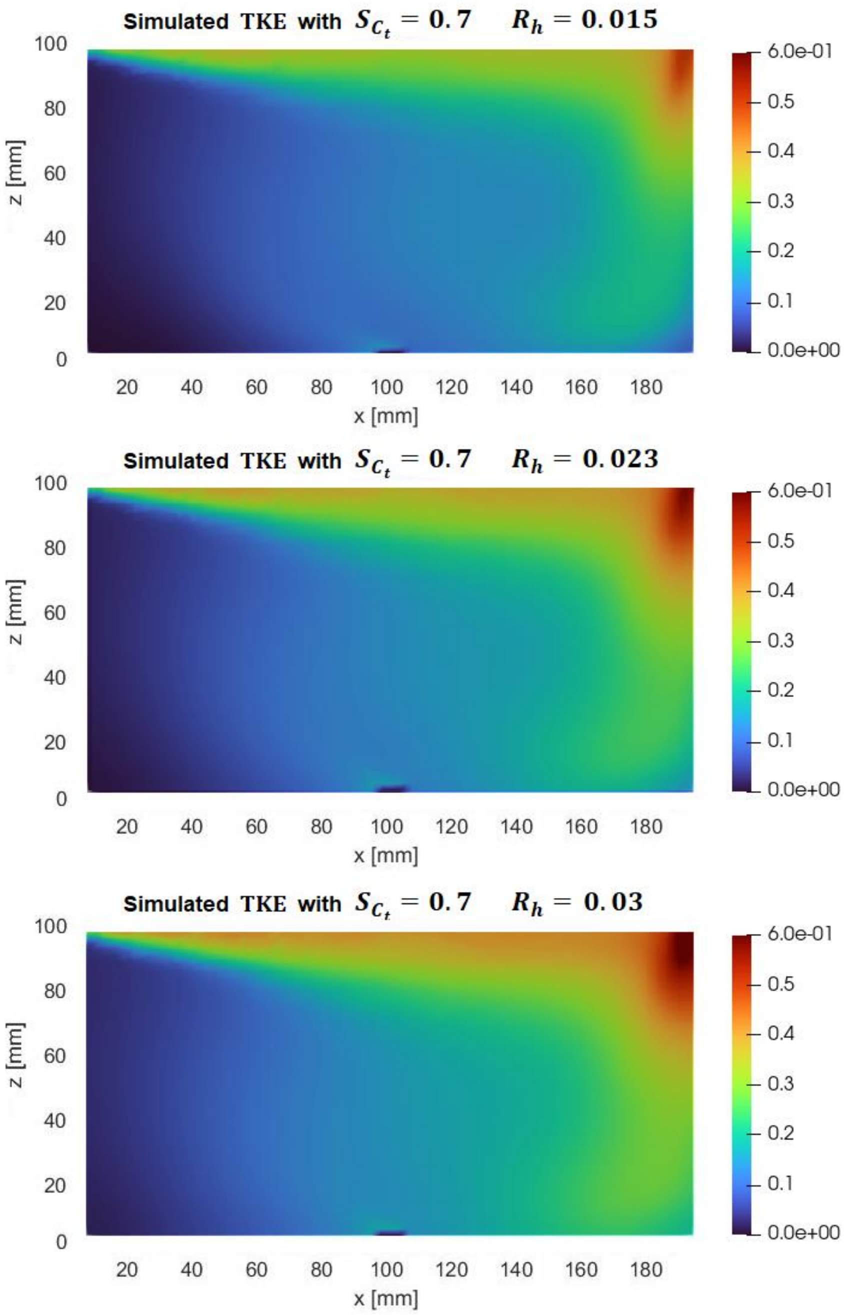


***Figure 3.3.4*** *– From the top to bottom, TKE* $[m^2/s^2]$ *obtained increasing roughness height with fixed Schmidt number* $S_{C_t} = 0.7$*. The fixed Schmidt number is the default value in Ansys Fluent i.e., the value of the base case highlighted in Figure 3.2.7.*

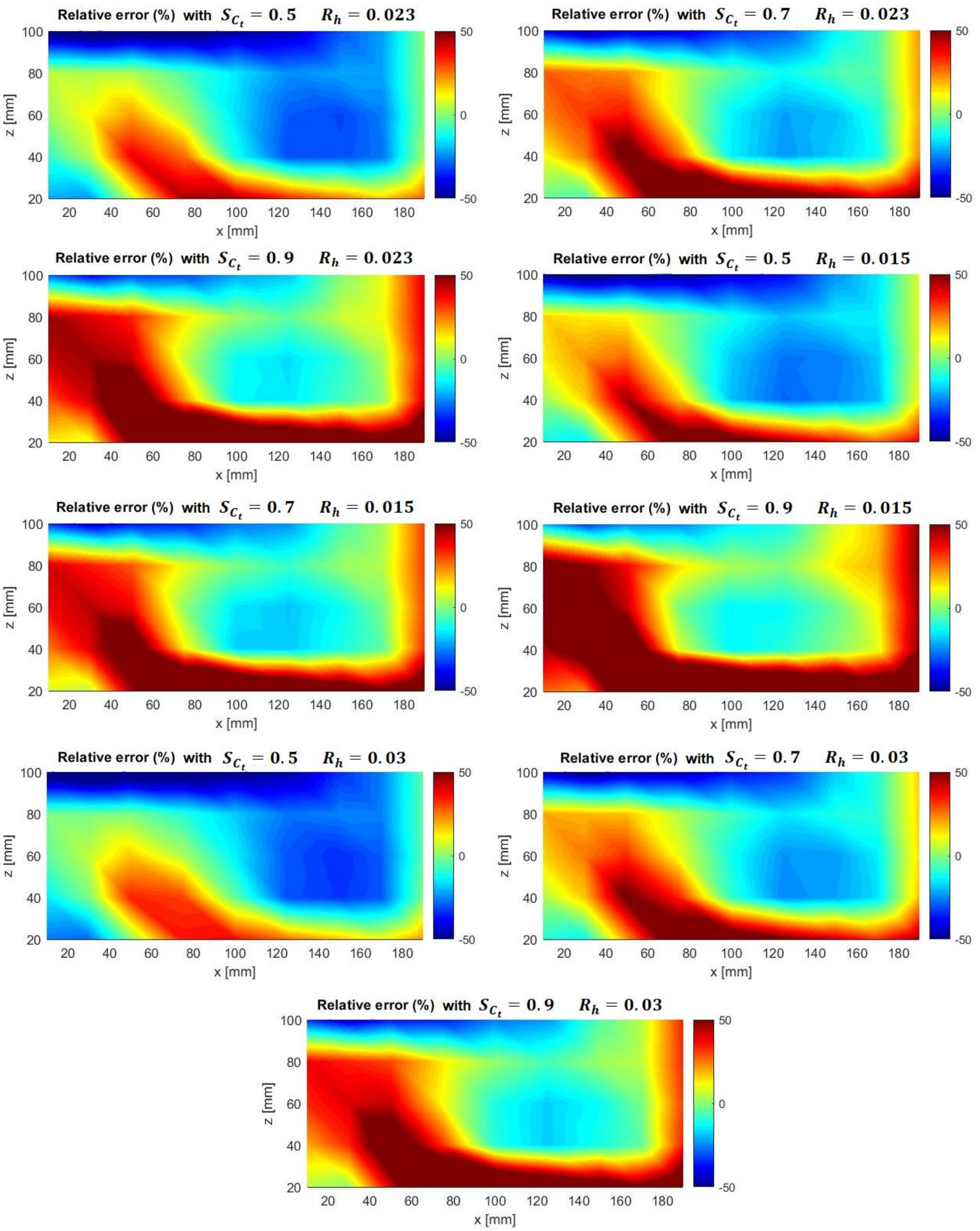


***Figure 3.3.5–*** *Relative percentage error committed on the estimation of the concentration field in all the carried-out simulations changing roughness height and Schmidt number. The error has been computed using the relation* $(c_{sim} - c_{exp})/c_{exp} \cdot 100$ *where* $c_{sim}$ *is the simulated concentration and* $c_{exp}$ *is the experimental concentration. In this way, positive percentage values indicate that the simulation overestimates the concentration and negative percentage values indicate that the simulation underestimates the concentration.*

*Figure 3.3.4* shows TKE field in the cavity increasing roughness height with fixed Schmidt number. These results extend the observation already done for TKE profiles in *Figure 3.3.1,* all over the cavity. In fact, higher values of roughness height lead to higher values of TKE in all the cavity*. Figure 3.3.5* shows the relative percentage error committed on the estimation of the concentration field in each case. These results confirm the observation reported above, i.e., high values of Schmidt number permit a good estimation of the concentration field in the right part of the cavity and low values of Schmidt number lead to a good estimation of the concentration field in the left part of the cavity.

A mean relative percentage error has been computed neglecting the overestimation or underestimation of the concentration field.

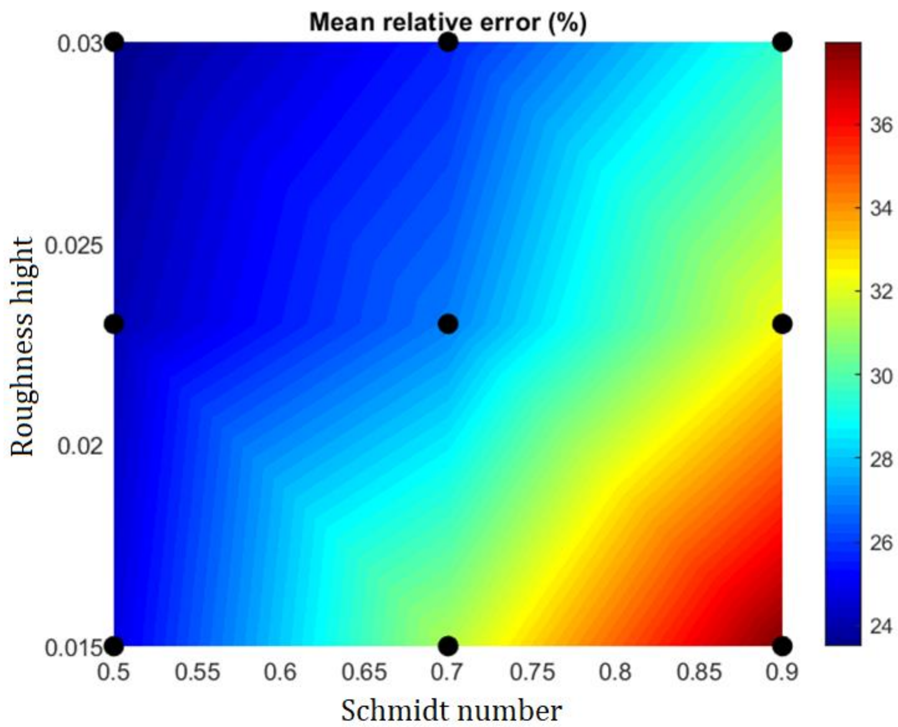


***Figure 3.3.6 –*** *Mean relative percentage error computed using the relation* $|c_{sim} - c_{exp}|/c_{exp} \cdot 100$*. The black points represent the combinations of Schmidt number and roughness height analysed in the carried-out simulations. This error computes the global accuracy of the simulation, furnishing only one percentage value, disregarding the overestimation/underestimation zones. The picture shows as, from this point of view, the best simulations are obtained for low value of Schmidt number and high values of roughness height.*

The results are shown in *Figure 3.3.6.* This has been done to select the better parameters to use to obtain a global qualitative representation of the concentration field as close as possible to the experimental results. The picture shows that the best results are obtained using lower values of Schmidt number and higher values of roughness height.

*Figure 3.3.7* shows vertical velocity and TKE profiles in the middle of the cavity, i.e., x = 100 mm, for the three different values of roughness height with fixed Schmidt number. The vertical velocity profiles result to be overestimated in the numerical simulations.

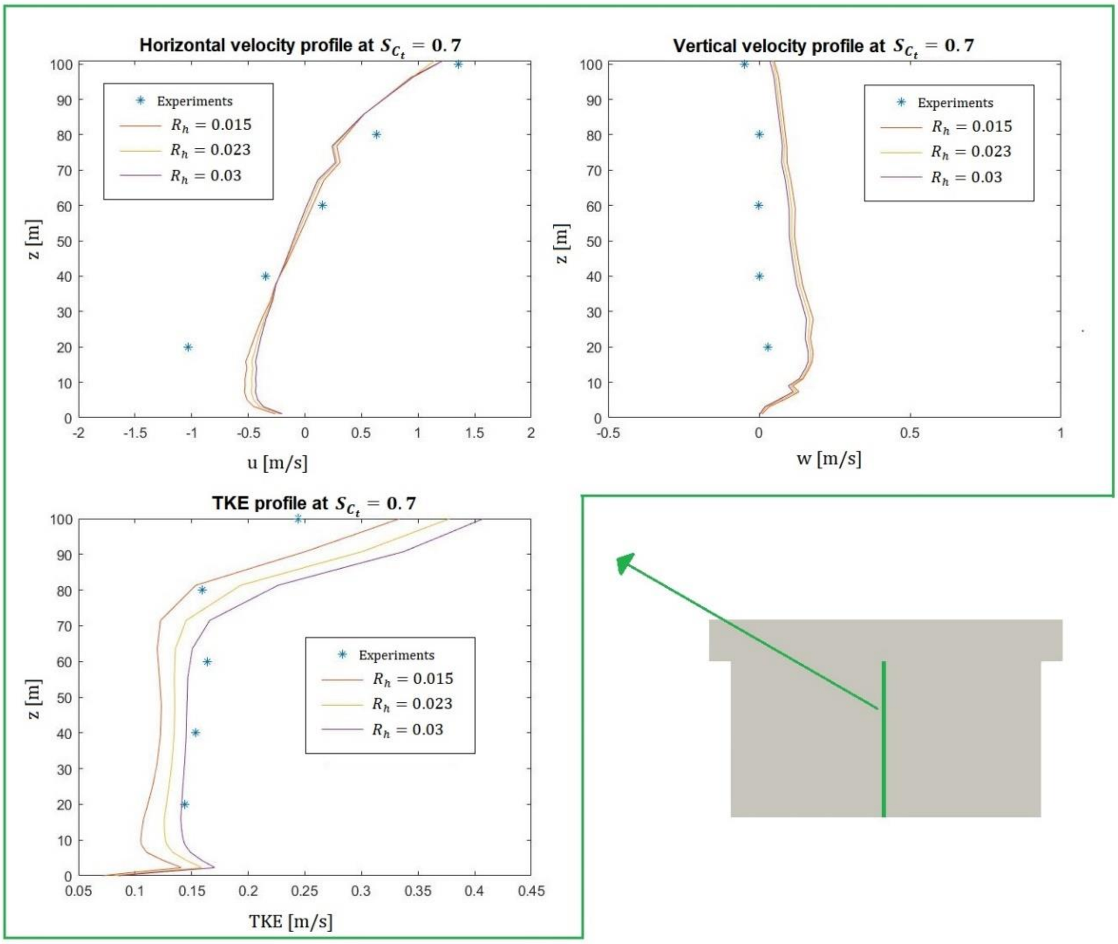


***Figure 3.3.7*** *– Horizontal and vertical velocity profiles (top) and TKE profiles (bottom left) in the middle of the cavity i.e., x = 100 mm, for different values of roughness height and fixed Schmidt number* $S_{C_t} = 0.7$. *The experimental profiles have been averaged along y.*

In particular, the simulated values remain positive along all the height, instead the experimental values are mostly near to zero except on the top of the cavity where a negative value is present. This suggests the presence of a recirculating cell coming out from the top of the cavity in the simulations. Furthermore, this suggests that in the simulations, the recirculating cell centre results to be shifted to right with respect to the centre of the cavity. Instead, the null experimental values in the middle of the cavity suggest a recirculating cell centre coinciding approximately with the cavity centre. These suggestions are confirmed by the results in *Figure 3.3.8,* where the streamlines of the mean velocity field are shown.

On the other hand, the horizontal velocity profiles, result to be underestimated near the source in the numerical simulations. This could explain the overestimation of the pollutant concentration near the source. In fact, low velocity inhibits the transport of pollutant emitted by the source from the bottom to the top of the cavity. TKE profiles result in a good agreement with the experimental values in the case with $R_h = 0.03$, except for the values on the top of the cavity that are overestimated.

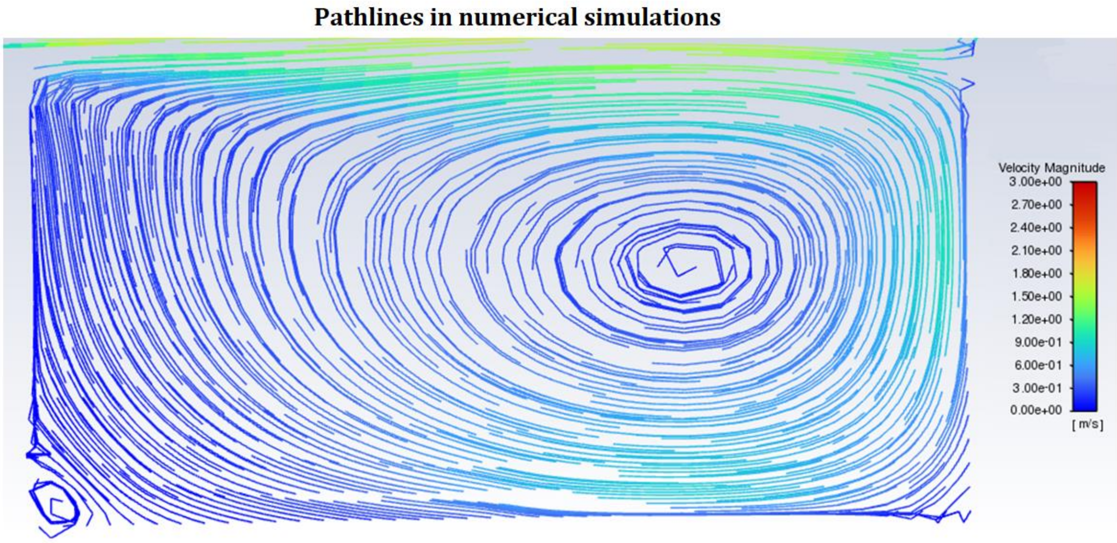


***Figure 3.3.8 –*** *Streamlines of the mean velocity field from the numerical simulations. The lines show the recirculating cell, shifted to right with respect to the centre of the cavity, as expected from velocity profiles shown in Figure 3.3.7. The colour of the lines indicates, as reported in the colorbar, the point-wise velocity magnitude in the cavity. A small secondary recirculating structure is also visible at the bottom left corner.*

Differently from the analysis on the concentration field, results on velocity profiles don't show any significant difference among the nine different combinations of parameters analysed in the simulations.

## 3.3.2 Configuration with trees

In this section, results for the configuration with trees are presented. The latter are modelled by means of two boxes of porous wood in order to use a solid material to represent the trees. Though not the ideal to mimic the real case, this option is commonly used to model the vegetation in Ansys Fluent. The available materials are wood and aluminium but, since no thermal effect and no heat exchanges with the surrounding environment are considered in this study, the two materials are equivalent. The porosity available in Ansys Fluent is the fluid porosity defined as the ratio between the volume of fluid and the total volume. In this sense, a fluid porosity equal to 1 means that all the zone is occupied by the fluid and, similarly, a fluid porosity equal to 0 means that all the zone is occupied by the solid. In this study, a fluid porosity equal to 0.05 is chosen. The reason of this choice lies in the measured experimental porosity. In fact, in the experimental campaign an optical porosity has been measured in order to characterize the trees. This optical porosity is defined in the same way with respect to the fluid porosity in Ansys Fluent, i.e., as the ratio between the volume not occupied by the crown of the tree (i.e., the fluid in Ansys Fluent) and the total volume. In the experiments an optical porosity equal to 0.05 has been measured. Nevertheless, it is important to notice that the shape and the material of the trees in the experiments and in the simulations are different. This could weaken the choice to use the same porosity definition, but the influence of these aspects is hardly quantifiable. In this sense, this is the most natural choice to model the porosity.

In *Figure 3.3.9* the simulated concentration field obtained for the three cases that better work for the configuration without trees are showed and compared to the experiment. As already discussed, the experimental concentration field in the configuration with the trees in strongly three-dimensional.

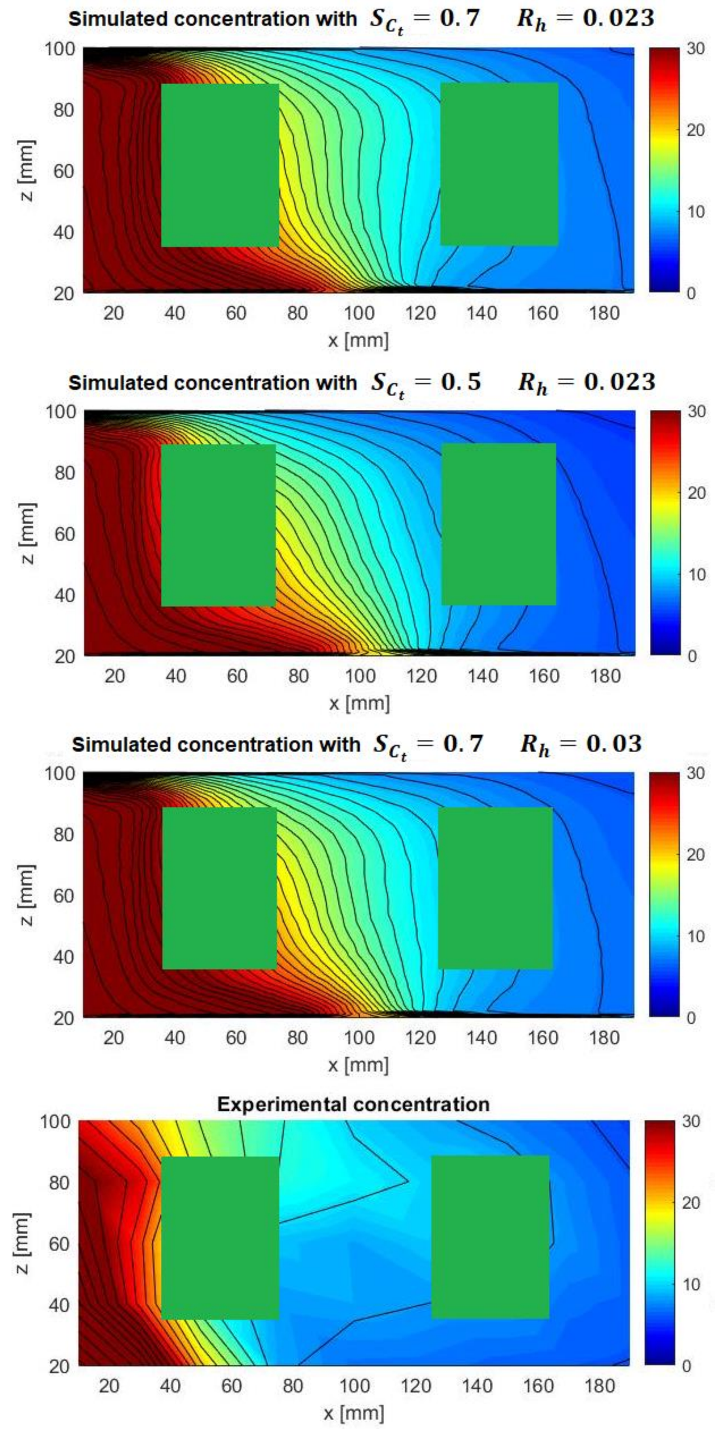


*Figure 3.3.9– From the top to bottom, concentration field obtained in the three cases that better work in the configuration without trees. Experimental concentration field at the bottom. In the experimental concentration field, green boxes have been placed to represent trees even if in the experiment the trees do not have this shape. This has been done to ease the comparison with the simulated concentration field. The experimental data are taken at the section placed at y = -280 mm.*

This allows the comparison with several sections in the direction $y$ along the cavity. In *Figure 3.3.9* the section that better matches the simulation is showed, i.e., $y = -280\ mm$. The numerical results show a higher concentration downwind the tree on the left of the cavity. In particular, as shown in *Figure 3.3.10, Figure 3.3.11 and Figure 3.3.12,* they are in good agreement with the experiment, except for the values near the source in the middle of the cavity. Here, the simulation overestimates the concentration. This result is also observable in the configuration without trees so is not due to the modelling of the trees but to the limits of the RANS approach.

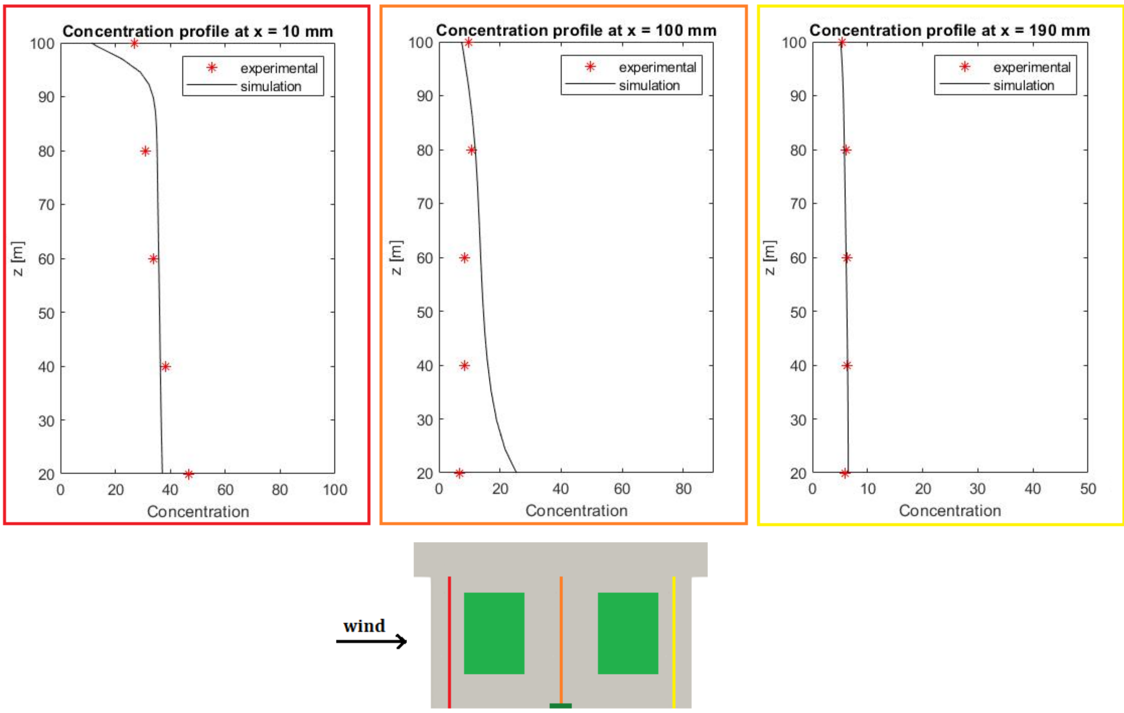


***Figure 3.3.10***– *Profiles of concentration field obtained in the case with Schmidt number* $S_{C_t} = 0.5$ *and roughness height* $R_h = 0.023$ *compared to experiments. Red, orange, and yellow lines represent the different positions along x direction in the cavity where the profiles are compared. The experimental data are taken at the section placed at y = -280 mm.*

In *Figure 3.3.13* profiles of velocity components and TKE are shown. The underestimation of the horizontal velocity near the source could be an explanation for the overestimation of concentration in the same zone. In fact, as already discussed for the configuration without trees, lower velocities inhibit the transport of pollutant emitted by the source.

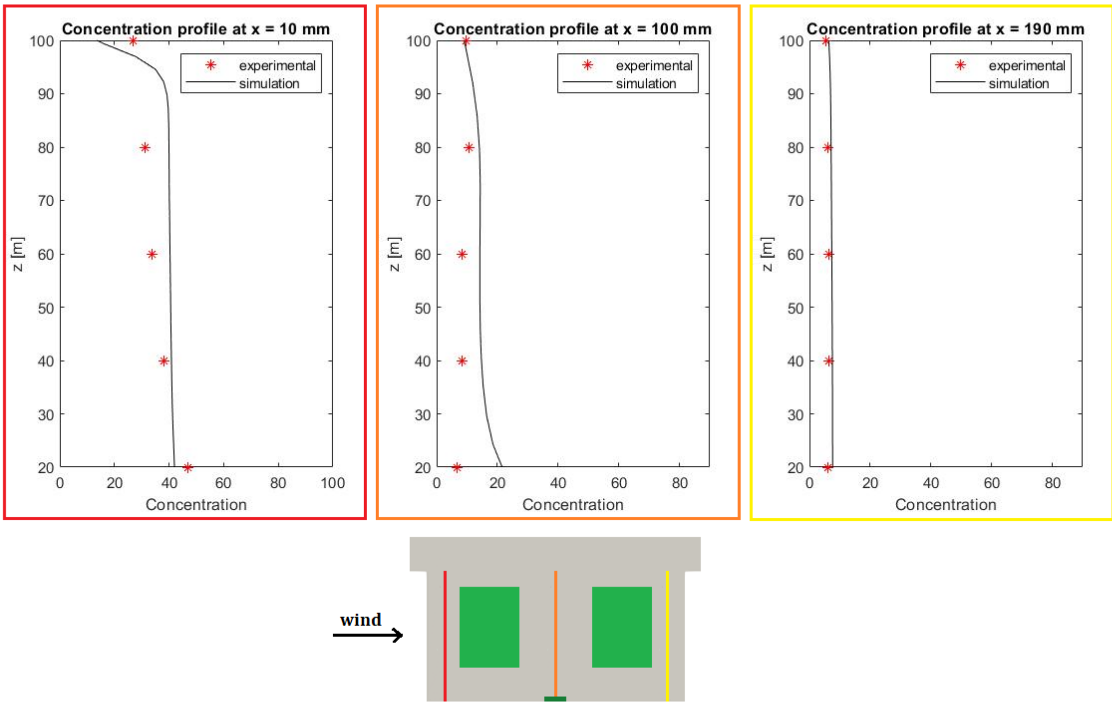


***Figure 3.3.11*** *– Profiles of concentration field obtained with Schmidt number* $S_{C_t} = 0.7$ *and roughness height* $R_h = 0.023$ *compared to experiments. Red, orange, and yellow lines represent the different positions along x direction in the cavity where the profiles are compared. The experimental data are taken at the section placed at y = -280 mm.*

To complete the analysis, *Figure 3.3.14* and *Figure 3.3.15* show the same results for the case with Schmidt number $S_{C_t} = 0.7$ and roughness height $R_h = 0.023$ compared with the experimental sections taken respectively where the minimum and maximum of the mean concentration field are measured. As expected, the comparison with the sections of minimum and maximum concentration in the experimental field shows respectively an underestimation and an overestimation in the simulated concentration field. These results point out the three-dimensionality of the concentration field and consequently the need of a three-dimensional numerical analysis.

Finally, *Figure 3.3.16* shows the streamlines of the mean velocity field. In particular, a main recirculating cell overall the cavity and a recirculating cell between the trees are present. Furthermore, a small secondary structure is present downwind the tree at the right of the cavity. As expected, the presence of trees alters the velocity field, breaking the main central structure which characterizes the empty cavity. In this way, this central structure splits into two new structures, one involving the zone surrounding the trees and another between the trees.

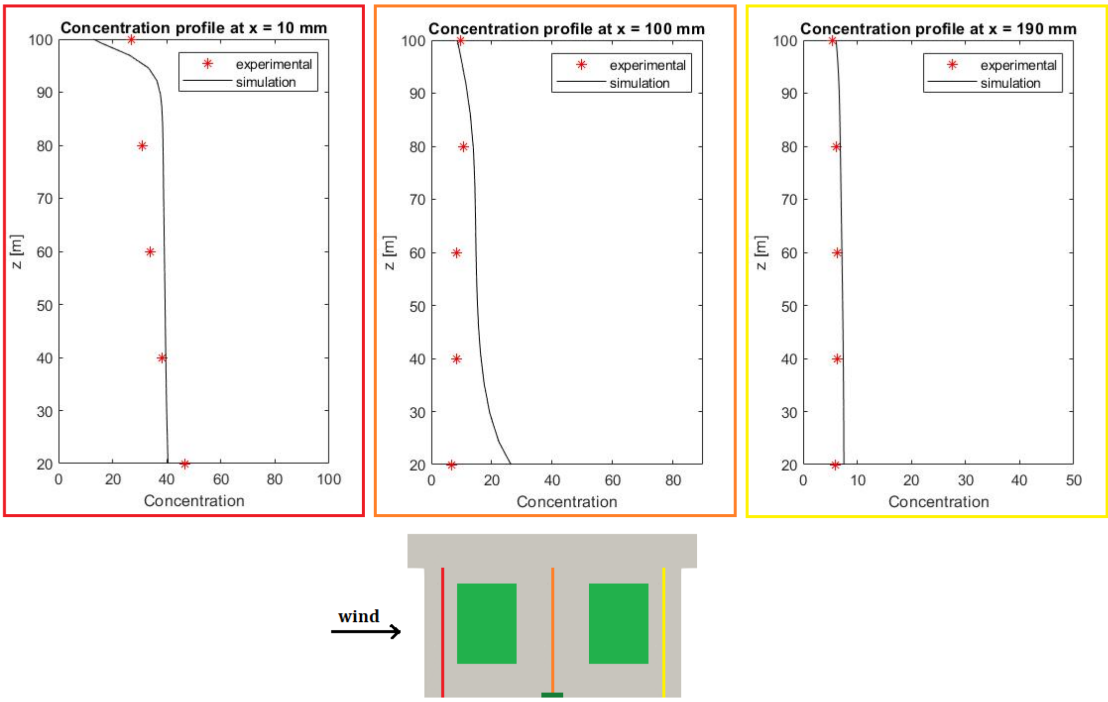


***Figure 3.3.12*** *– Profiles of concentration field obtained with Schmidt number* $S_{C_t} = 0.7$ *and roughness height* $R_h = 0.03$ *compared to experiments. Red, orange, and yellow lines represent the different positions along x direction in the cavity where the profiles are compared. The experimental data are taken at the section placed at y = -280 mm.*

The main weakness in all the realized simulations has been the difficulty in reproducing the concentration and velocity field near the source. Different aspects have been evaluated to face this problem, starting from the changings in the roughness length of the wall and ending up with a refinement of the mesh near the wall. *Figure 3.3.17* shows the profiles of the concentration field for the three meshes tested, as indicated in section 3.2.1. The results are compared to the experiment along the profile placed at the centre of the cavity, i.e., on the source. It is immediate to notice that a refinement of the mesh improves the results of the simulation. Anyway, the improvement obtained with the finest mesh is not enough significant to justify the additional computational cost.

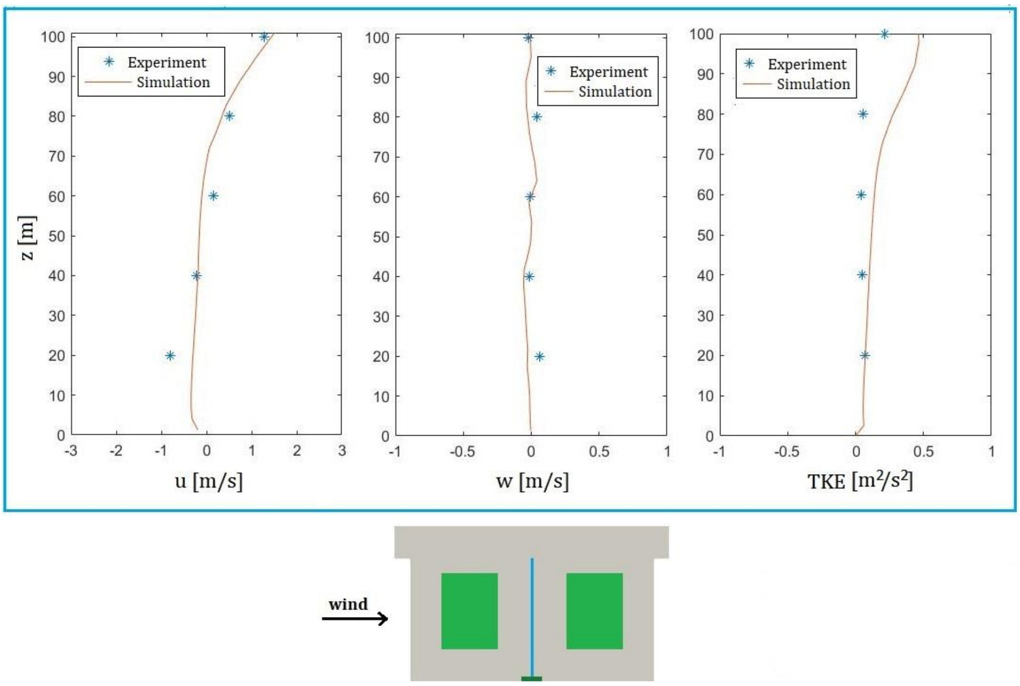


*Figure 3.3.13– Profiles of velocity components and TKE obtained in the case with Schmidt number $S_{C_t} = 0.7$ and roughness height $R_h = 0.023$ compared to experiments. The profiles are compared in the middle of the cavity, i.e., x = 100 mm. The experimental data are taken at the section placed at y = -280 mm.*

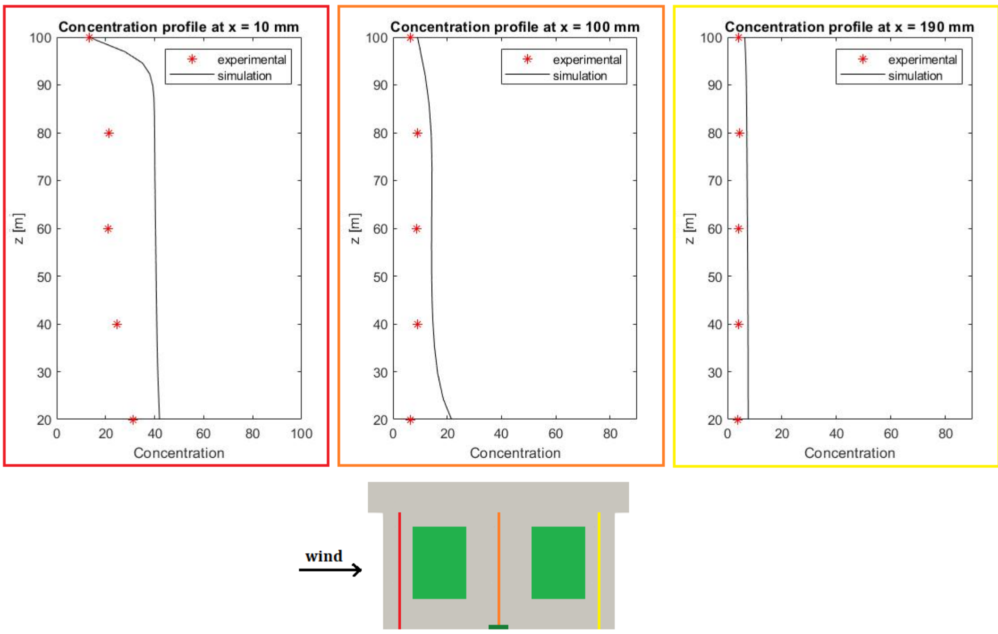


*Figure 3.3.14– Profiles of concentration field obtained in the case with Schmidt number $S_{C_t} = 0.7$ and roughness height $R_h = 0.023$ compared to experiments. Red, orange, and yellow lines represent the different positions along x direction in the cavity where the profiles are compared. The experimental data are taken at the section of minimum concentration field, i.e., y = 0 mm.*

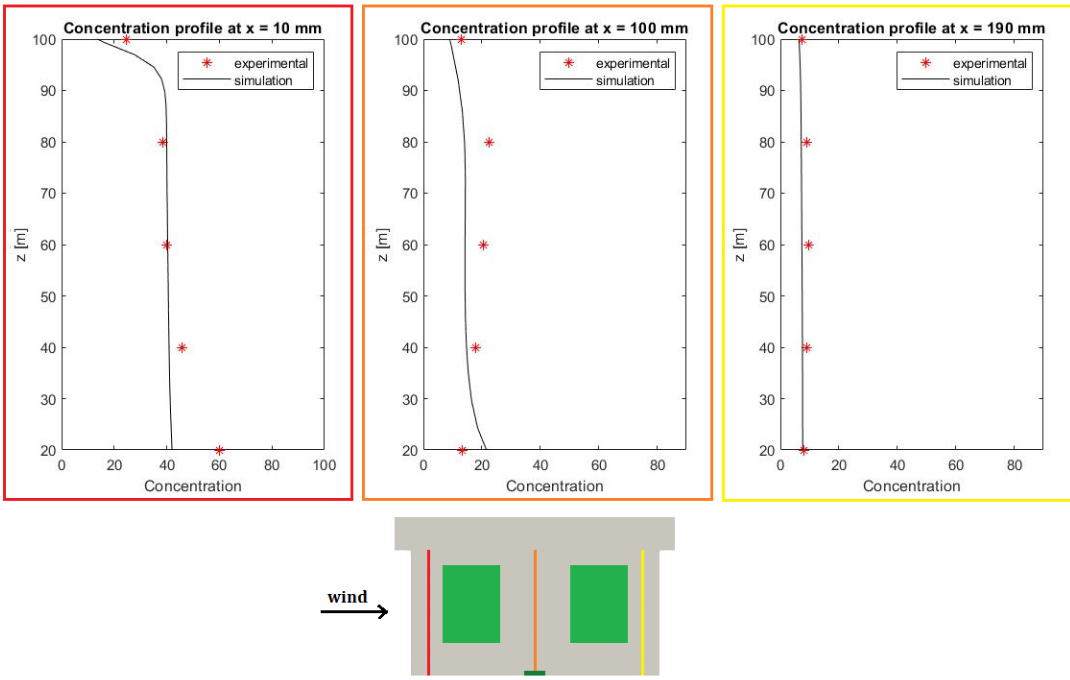


***Figure 3.3.15*** *– Profiles of concentration field obtained in the case with Schmidt number $S_{C_t} = 0.7$ and roughness height $R_h = 0.023$ compared to experiments. Red, orange, and yellow lines represent the different positions along x direction in the cavity where the profiles are compared. The experimental data are taken at the section of maximum concentration field, i.e., y = 215 mm.*

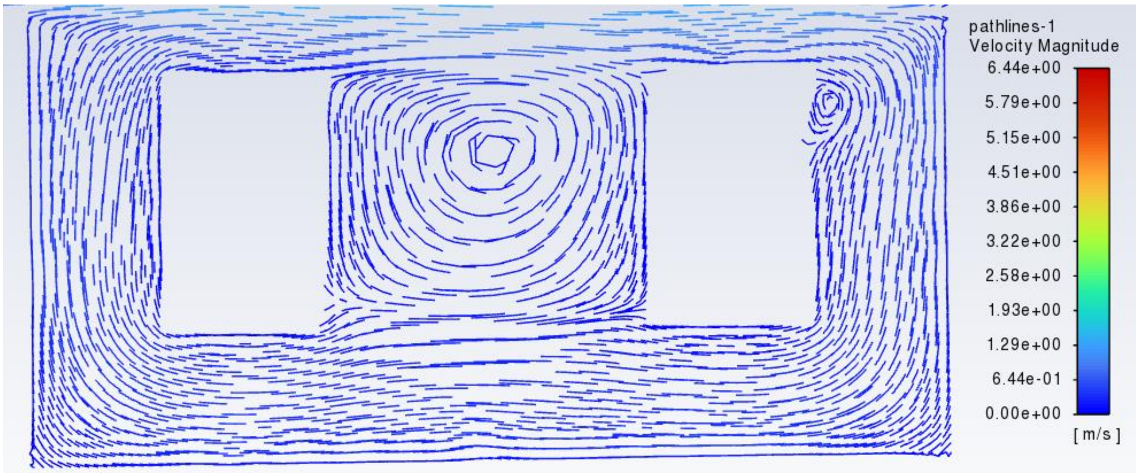


***Figure 3.3.16*** *– Streamlines of the mean velocity field from the numerical simulation. The lines show the recirculating cell between the trees. The colour of the lines indicates, as reported in the colorbar, the point-wise velocity magnitude in the cavity. A small secondary recirculating structure is also visible downwind the tree at the right of the cavity.*

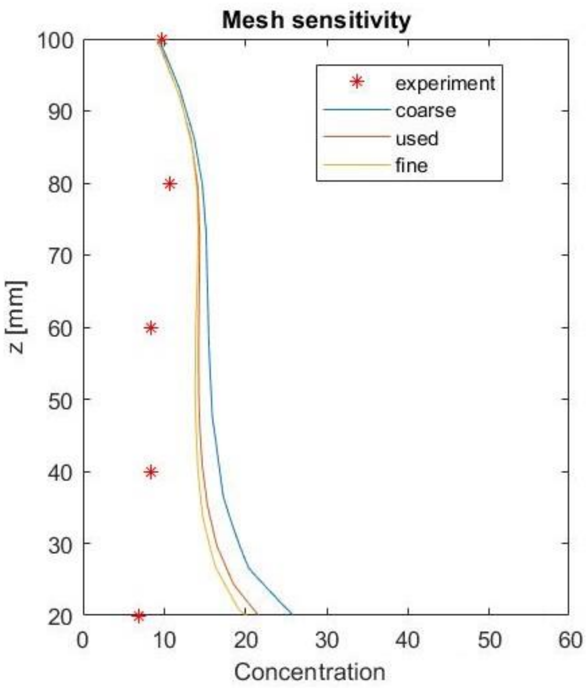


***Figure 3.3.17***– *Profiles of concentration field obtained for meshes of different refinement. The profiles are compared to the experiment in the middle of the cavity, i.e., on the source. The experimental data are taken at the section placed at y = -280 mm.*

# Conclusions

The aim of this work has been to advance the understanding of the effect of vegetation on the dispersion of pollutants in urban canyons. This has been done by means of an experimental campaign and RANS numerical simulations.

Concerning the experimental results, two main different aspects have been considered and analysed: the concentration field and vertical exchange velocity between the canyon and the surrounding environment. Differently from some of the previous studies, the urban canyon has been set up as a closed cavity and this has made possible a good estimation of the vertical exchange velocity due to the perfect balance between the quantity of ethane-air mixture emitted by the source and the quantity coming out from the top of the cavity.

The results have shown how the presence of trees modifies the pollutant concentration field. In particular, the configuration without trees resulted in a homogeneous concentration field along the main axis of the cavity, i.e., perpendicular to the wind direction. For this reason, the concentration field can be considered nearly two-dimensional. The two configurations with trees instead, presented an inhomogeneous concentration field, suggesting the presence of more complicated flow structures and different turbulent scales. Both the configurations analysed presented two concentration peaks along the canyon axis. In particular, the half configuration seemed to be characterized by a more homogenous concentration field with respect to the full configuration between these two peaks. This suggested the presence of a more turbulent flow field in the half configuration allowing a better mixing.

Furthermore, the results obtained computing the vertical exchange velocity did not show any significant difference among the configurations analysed, therefore suggesting that the presence of trees does not affect the ventilation in the canyon.

The carried-out numerical simulations pointed out the limits of the RANS approach in modelling flow within complex geometries and therefore characterized by complex turbulent structures. Nevertheless, it is useful to underline its capability to capture the most relevant aspects of the flow field using a very low computational cost. The work opens several future perspectives on both the experimental and numerical sides. In particular, the obtained experimental results have brought awareness of the need to carry out velocity measurements to characterize the structure of the flow field and to better understand the causes of the peaks observed in the concentration field in presence of trees. On the numerical side instead, the results have suggested an improvement of the accuracy of the numerical simulations, motivating the realization of three-dimensional Large-Eddy Simulation in order to resolve the turbulence scales which contain the great part of the total energy. Furthermore, the study of different trees configurations, of a different aspect ratio for the canyon, of different tree porosity and trees shape and dimension would be certainly interesting. Finally, another important aspect to take into account in future studies could be the characterization of the thermal exchange between the trees and the surrounding environment. This allow to consider the trees as living entities as in the real case and to take into account their important role in climate regulation.

# References

Balestrieri, G. (2021). *Influence of vegetation on vertical mass exchange velocity in urban street canyon*. PhD thesis, Politecnico di Torino.

Buccolieri, R., Gromke, C., Di Sabatino, S., and Ruck, B. (2009). *Aerodynamic effects of trees on pollutant concentration in street canyons*. Science of the Total Environment, 407(19):5247–5256.

Cancelli, C., Boffadossi, M., and Salizzoni, P. (2006). *Fluidodinamica ambientale: Turbolenza e dispersione*. Otto Editore.

De Giovanni, A. (2019). *Assessment of the impacts of trees on pollutants dispersion in urban canopy by means of a wind tunnel study*. PhD thesis, Politecnico di Torino.

Fellini, S. (2021). *Modelling pollutant dispersion at the city and street scales*. PhD thesis, École Centrale de Lyon.

Fellini, S., Ridolfi, L., and Salizzoni, P. (2020). *Street canyon ventilation: Combined effect of cross-section geometry and wall heating*. Quarterly Journal of the Royal Meteorological Society, 146(730):2347–2367.

Grilo, F., P. Pinho, C. Aleixo, C. Catita, P. Silva, N. Lopes, C. Freitas, M. SantosReis, T. McPhearson, and C. Branquinho (2020). *Using green to cool the grey: Modelling the cooling effect of green spaces with a high spatial resolution*. Science of the Total Environment 724, pp. 1–10.

Gromke, C., Buccolieri, R., Di Sabatino, S., and Ruck, B. (2008). *Dispersion study in a street canyon with tree planting by means of wind tunnel and numerical investigations–evaluation of cfd data with experimental data*. Atmospheric

Environment, 42(37):8640–8650.

Gromke, C. and Ruck, B. (2009). *On the impact of trees on dispersion processes of traffic emissions in street canyons*. Boundary-Layer Meteorology, 131(1):19–34.

Gromke, C. and Ruck, B. (2012). *Pollutant concentrations in street canyons of different aspect ratio with avenues of trees for various wind directions*. Boundary-Layer Meteorology, 144(1):41–64.

Guan D., Zhang Y., Zhu T., *A wind-tunnel study of windbreak drag*. Agricultural and Forest Meteorology 118.1-2 (2003); 75-84.

Salizzoni, P., Soulhac, L., and Mejean, P. (2009). *Street canyon ventilation and atmospheric turbulence*. Atmospheric Environment, 43(32):5056–5067.

Wilcox D.C. (1998), *Turbulence modelling for CFD*. DCW Industries Inc., California.